



Article

Building Function Type Identification Using Mobile Signaling Data Based on a Machine Learning Method

Wenyu Nie ^{1,2}, Xiwei Fan ^{1,2,*}, Gaozhong Nie ^{1,2}, Huayue Li ^{1,2,3} and Chaoxu Xia ^{1,2}¹ Key Laboratory of Seismic and Volcanic Hazards, China Earthquake Administration, Beijing 100029, China² Institute of Geology, China Earthquake Administration, Beijing 100029, China³ China Earthquake Networks Center, Beijing 100045, China

* Correspondence: fanxiwei@ies.ac.cn

Abstract: Identifying building function type (BFT) is vital for many studies and applications, such as urban planning, disaster risk assessment and management, and traffic control. Traditional remote sensing methods are commonly used for land use/cover classification, but they have some limitations in BFT identification. Considering that the dynamic variations of social sensing mobile signaling (MS) data at diurnal and daily scales are directly related to BFT, in this paper, we propose a method to infer BFT using MS data obtained from mobile devices. First, based on the different patterns of population dynamics within different building types, we propose a BFT classification scheme with five categories: residential (*R*), working (*W*), entertainment (*E*), visiting (*V*), and hospital (*H*). Then, a random forest (RF) classification model is constructed based on two days (one workday and one weekend) of MS data with a temporal resolution of one hour to identify the BFT. According to the cross-validation method, the overall classification accuracy is 84.89%, and the Kappa coefficient is 0.78. Applying the MS data-constructed RF model to the central areas of Beijing Dongcheng and Xicheng Districts, the overall detection rate is 97.35%. In addition, to verify the feasibility of the MS data, the Sentinel-2 (S2) remote sensing data are used for comparison, with a classification accuracy of 73.33%. The better performance of the MS method shows its excellent potential for BFT identification, as the spatial and temporal population dynamics reviewed based on MS data are more correlated with BFT than geometric or spectral features in remote sensing images. This is an innovative attempt to identify BFT with MS data, and such a method compensates for the scarcity of BFT studies driven by population dynamics. Overall, in this study, we show the feasibility of using time series MS data to identify BFT and we provide a new path for building function mapping at large scales.

Keywords: building function type; mobile signaling data; random forest; Sentinel-2; population dynamics

Citation: Nie, W.; Fan, X.; Nie, G.; Li, H.; Xia, C. Building Function Type Identification Using Mobile Signaling Data Based on a Machine Learning Method. *Remote Sens.* **2022**, *14*, 4697. <https://doi.org/10.3390/rs14194697>

Academic Editors: Prashant Kumar, Amin Anjomshoaa and Markus Helfert

Received: 26 July 2022

Accepted: 16 September 2022

Published: 20 September 2022

Publisher's Note: MDPI stays neutral with regard to jurisdictional claims in published maps and institutional affiliations.



Copyright: © 2022 by the authors. Licensee MDPI, Basel, Switzerland. This article is an open access article distributed under the terms and conditions of the Creative Commons Attribution (CC BY) license (<https://creativecommons.org/licenses/by/4.0/>).

1. Introduction

With the continuous development of the economy and society, buildings have become important carriers supporting human activities. More people are living in city areas as urbanization progresses [1]. As the basic structural unit of construction and human activities, buildings are the key elements that support citizens' living, working, recreation, and other social activities. The diversity of building function type (BFT) is a significant indicator of the evolution of urban civilization, and its rational planning is crucial for human well-being. In recent years, BFT has attracted widespread academic attention in multiple fields, such as urban planning, disaster assessment, and environmental monitoring [2,3]. However, the acquisition of BFT traditionally requires researchers to investigate a site in person or distribute lengthy questionnaire reports, which are expensive, time-consuming, slow to update, and difficult to implement in large areas. Therefore, some methods that are low cost, easier to use, and can be applied to large areas are crucial for BFT acquisition.

In recent years, studies of BFT identification have mostly used remote sensing or social sensing data [4]. Remote sensing data are mainly acquired from space-borne/airborne/

ground-based (street view) remote sensors, while social sensing data are commonly obtained from people's or vehicles' portable sensors, such as smartphones or smart wearables. These two types of data collect information on city or village areas from different perspectives through remote sensors or human sensors and generate BFT products from physical or human points of view, respectively, according to different application purposes. The methods that solely use one type or a combination of data are widely used for BFT identification with promising results [4–6]. However, few studies have directly linked BFT identification with mobile signaling (MS) data to produce BFT products driven by population dynamics. In this study, we aim to explore the potential of MS data to construct the relationship between population dynamics at diurnal and daily scales and BFT. In addition, as few studies have used MS data alone to identify large-scale BFTs, in this study, remote sensing data from Sentinel-2 (S2) are used for comparison to prove the feasibility and advancement of the proposed MS-based method.

In addition to the data being used, the identification method is another important component of BFT classification research. With the rapid development of artificial intelligence and computer technology, machine learning methods have been used in a wide range of applications, such as urban function classification [7], disaster detection [8,9], and risk assessment [10]. As the demand for data analytics continues to grow in the big data era, how to carry out deep analyses of complex and diverse data based on machine learning and use information more efficiently has become the main direction of machine learning research in the current big data environment. In terms of mathematical functions, the classification task is to obtain an objective function (f) by learning to map each attribute set (x) to a predefined class label (y), that is, we obtain a classification model (i.e., obtain a function between sample attributes and class labels) based on some known samples (including attributes and class labels), and then classify the sample data containing only attributes by this objective function. This is the most commonly used classification scenario for machine learning and the basic principle for BFT classification in this study, i.e., constructing a function between the time-series attributes of the population and the BFT based on some known samples to identify the BFT.

In this framework, the proposed approach introduces OpenStreetMap (OSM) data, and the street view of Gaode Map as the real BFT reference data to build a random forest (RF) classification model based on the proposed population dynamics-oriented BFT classification framework. This work focuses on the classification of buildings according to the given BFT classification scheme. Through an accurate evaluation and comparison with remote sensing data methods, we demonstrate that MS data can be used to identify different functional types of urban buildings with reasonable accuracy. To this end, the potential of MS data to reflect population dynamics is discussed, and qualitative and quantitative evaluations are performed for several MS indicators to select the optimal metrics for the BFT classification model. Then, the classification results and their applications are described in detail.

The innovative contributions of this study are mainly in two areas. First, based on the time-series information, this is the first attempt to use a special type of social sensing MS data in urban BFT identification. As compared with other types of social sensing data, MS data have the advantages of full spatial coverage and a high penetration rate, which provide an effective database for large-scale BFT mapping. The high penetration rate of mobile devices results in MS data that reflect human dynamics at a high temporal resolution. The high temporal resolution time-series information used for BFT identification is the key point as compared with other social sensing-based methods. As compared with traditional widely used satellite remote sensing data, MS data have the advantages of being intrinsically more useful for BFT identification, as population spatial and temporal dynamic variations reviewed by MS data are more correlated with BFT than geometric or spectral features in remote sensing images. Second, the building function classification scheme proposed in this study is driven by population dynamics at diurnal and daily scales. Considering that the MS data are directly correlated with population spatial and temporal dynamics, which are mostly determined by BFTs, the building function classification scheme is proposed,

and BFT is estimated based on population dynamics shown as time-series MS data on two days (workday and weekend). Committed to referencing and improving the original classification scheme, we have created a building function classification product based on population dynamics variation patterns. In the era of exploding population growth, this BFT product is of great importance in urban planning, management, and emergency response.

This paper is structured as follows: In Section 2, we review previous work related to the addressed topics; in Section 3, we describe the study area and data used in this study are provided; the data preprocessing and RF model construction are described in Section 4; the results are presented in Section 5; in Section 6, we discuss the results; and in Section 7, we provide the conclusions of this study.

2. Previous Work

This study aims to develop a new approach to identify BFT in terms of population dynamics, which has significant implications for urban planning and management. In this section, we review the latest techniques related to the identification of the urban functions, focusing on the data and methods developed for urban BFT identification, and discuss in detail the significance of MS data for the indication of population dynamics and investigate the mechanisms of its role in BFT mapping over a large scale and its potential applications. In addition, the application of machine learning is briefly discussed in relation to the research objectives of this paper.

The urban system is composed of different forms of functional areas, which Jane et al. has described as “organized complexity” [11]. Rodrigue et al. argued that there were two ways of defining urban land use: One definition focused on the forms and patterns of land use and was called formal land use; the other definition was based on a spatial socioeconomic description and was called functional land use [12,13]. The latter definition had a stronger population dependency and a higher level of dynamic variation than the former definition. Due to its high relevance to population dynamics, researchers have become increasingly interested in urban functional identification.

Currently, the two mainstream ways of identifying urban functional types are remote sensing and social sensing-based methods. Remote sensing-based methods typically use features extracted from remote sensing images, such as geometric, spectral, and texture features, to estimate urban functions [14,15]. Since the 1960s, remote sensing-based methods have been considered to be efficient for the identification of various terrestrial features. Improvements in sensors’ spatial, radiometric, and spectral properties have led to an era of high-quality optical images [16,17]. High-resolution remote sensing imagery provides rich and detailed image information that greatly facilitates large-scale environmental monitoring [18]. The prolonged study history and abundant archive data provide considerable convenience for land use/cover classification [19–21] and damage assessment and evaluation applications [22]. With the continuous development of industrialization and urbanization, most human activities have become concentrated in buildings. Thus, in recent years, more studies have turned their attention to BFT identification based on remote sensing images. Belgiu et al. extracted building types from airborne laser scanner data by implementing object-based image analysis method [23]. Xie et al. successfully classified three BFTs from high spatial resolution images using extended multiresolution segmentation and soft classification based on backpropagation networks [5]. Hoffmann et al. used aerial and street view images to classify urban BFTs into four categories, with an overall accuracy (OA) of 76% [17].

However, since large area satellite remote sensing is generally a vertical observation, only information on the roofs of buildings can be obtained. Note that most buildings are constructed from limited types of materials and shapes, and buildings with abundant functional types can be confused in spectral or geometric domains. Thus, remote sensing images often have difficulty reflecting detailed information about BFT due to the limitations of the remote sensing imaging mechanism [24]. Therefore, remote sensing-based methods

are usually used for urban functional area identification rather than building function identification [4].

With the enrichment of data resources and progress in processing techniques, social sensing-based methods have become another important branch for BFT identification. Different from remote sensing-based methods, current social sensing-based methods commonly use population dynamics to infer BFT. Social sensing data include taxi trajectories, points of interest (POI)s, social media data, data from WeChat and Weibo, and call detail records. These new datasets contain rich information on urban human activities and interactions [25,26]. Currently, there is growing literature using social sensing data for urban building functional mapping. Zhong et al. established a two-step framework making use of the spatial relationships between trips, stops, and buildings to infer building functions [13]. Niu et al. integrated multisource big data (WeChat, taxi trajectories, POIs, and building footprint data) to infer building functions in Guangzhou, China [2]. Zhang et al. proposed a data-driven approach that used station-based public bicycle rental records together with POI data in Hangzhou, China, to identify urban functional zones [27]. However, the data used in those studies have some obvious limitations: heterogeneous spatial sampling and relatively low sampling rates. For example, taxi trajectory, public transportation, and bike-sharing data are denser and more effective in large cities, but there are few data available in suburbs or villages. POI data are distributed mainly in densely populated areas and are more inclined to shopping, retail or central business districts, while residential areas are rare. Although WeChat, Twitter, and Weibo data have enormous numbers of users, the spatial and temporal resolutions are too coarse for BFT identification by analyzing the diurnal variations in population dynamics.

Considering these issues, in many studies, attempts have been made to infer building functions using multiple sources of big data. An increasing number of studies have combined remote sensing images with social sensing data for BFT identification, such as POI data [28], Twitter text messages [29], and geospatial data [30]. The combined use of multisource data has indeed enhanced the understanding and identification of urban functions. Gong et al. reported a nationwide land use map using data fusion of 10-meter satellite images, OSM data, nighttime lights, POIs, and Tencent data, and this result marked the beginning of a new approach to collaborative urban land use mapping over large areas [31]. However, for BFT identification, the fusion of multiple data would undoubtedly increase the workload and greatly increase the cost of mapping, and there are always limitations in large-scale applications. In addition, while multiple sources of data offer unprecedented opportunities for urban research, they also come with the problem that multiple sources of data may not fit well with each other [32]. For example, a park building in the center of a city may have sparse POIs but high-density taxi trajectories or geotagged social media content. This situation may cause misclassification of the BFT. The semantic bias of multiple data makes it difficult to unify the judgement criteria, and a combination of techniques is undoubtedly needed to solve this problem.

To address these limitations, emerging social sensing data, i.e., MS data, have attracted considerable attention from geoscience scholars. MS refers to the protocol control signals sent between a device and the network, which are used in mobile communication systems to transmit user information and ensure proper communication. These signals include data such as the numbers of active communication stations (Station), online mobile devices (Gid), active Wi-Fi hotspots (Wifimac), and connected devices in wireless networks (Loginmac) [33]. As of 2020, the penetration rate of mobile devices in China reached 112.91 per 100 people. The advantages of wide coverage, near real-time observation, and relatively high sample rate make it possible to use MS data for human activity-related studies. González et al. studied data from nearly 100,000 anonymous mobile device users and revealed persistent patterns in the statistical properties of human mobility [34]. Similarly, Song et al. highlighted the remarkable predictability of human activities, and argued that it was possible to predict a user's dynamics with 93% accuracy using mobile phone data alone [35]. As compared with other social sensing data datasets, MS data offer several advantages in urban functional

identification: (1) high penetration rate, (2) broad spatial coverage, and (3) rich information on human activities (high temporal resolution). Currently, these data have been applied to many areas, such as land use/land cover identification [7], service radius assessment of public facilities [36], and earthquake emergency response and rescue [37,38]. To date, few studies have tried to use MS data for urban BFT identification, even considering the significant correlations of MS data with variations in population dynamics.

Notably, previous social sensing data-based methods have focused on applying population spatial dynamics for BFT identification, and temporal information has not been well used. Montgomery et al. noted that the urban area should be an open space that harbors high-density human daily activities [39,40]. Rodrigue et al. defined these daily activities as routine activities performed during a 24-h day [12], and previous studies have shown that individuals usually had stable mobility patterns [41–44]. These studies have demonstrated the potential of using population temporal dynamics to infer different BFTs. Thus, in this paper, we aim to study the possibility of using time-series MS data for BFT identification.

Given the reliable performance of machine learning methods on classification problems, some BFT classification methods have been proposed based on artificial neural networks [45], convolutional neural networks [46], as well as random forest [7] and support vector machine [47,48] algorithms. The ability of machine learning methods to automatically learn high-level features from large amounts of data provides an effective reference for the classification of urban buildings. The RF classification algorithm is a decision tree-based machine learning algorithm [49]. Numerous theoretical and empirical studies have demonstrated that the RF algorithm has high prediction accuracy and good tolerance for outliers and noise and is not prone to overfitting [50]. The algorithm has been widely used in various fields for its excellent classification performance. Thus, in this study, we attempt to apply MS data based on the RF algorithm for BFT identification.

Considering these issues, we attempt to use time-series MS data to infer BFT, and therefore, propose a new BFT classification method based on information about urban functions reflected by patterns of population dynamics, with the technical support of RF machine learning methods. We believe that the classification product generated by our research is an innovative product at the population dynamics level and has important implications for urban planning and emergency management.

3. Study Area and Data Source

3.1. Study Area

Considering its high building density and inclusion of all types of BFTs, Beijing, the capital of China, is taken as the study area. The outer rectangular area of the Dongcheng and Xicheng Districts of Beijing, with an area of approximately 158 km², as indicated by the red box in Figure 1, is used for the RF model training and accuracy assessment. Located in the center of Beijing, it is the most iconic area of the city and the core of the capital's functions. With its dense population, high building density, and a full range of BFTs, this area can serve as an ideal region for studying the function types of buildings. In addition, from the data source point of view, there are more high-quality MS data of Beijing than those of other areas as more people live in Beijing and more mobile devices are being used. The rectangular area of the fifth ring of Beijing, as shown in the blue box of Figure 1, is taken as an example of the actual model application.

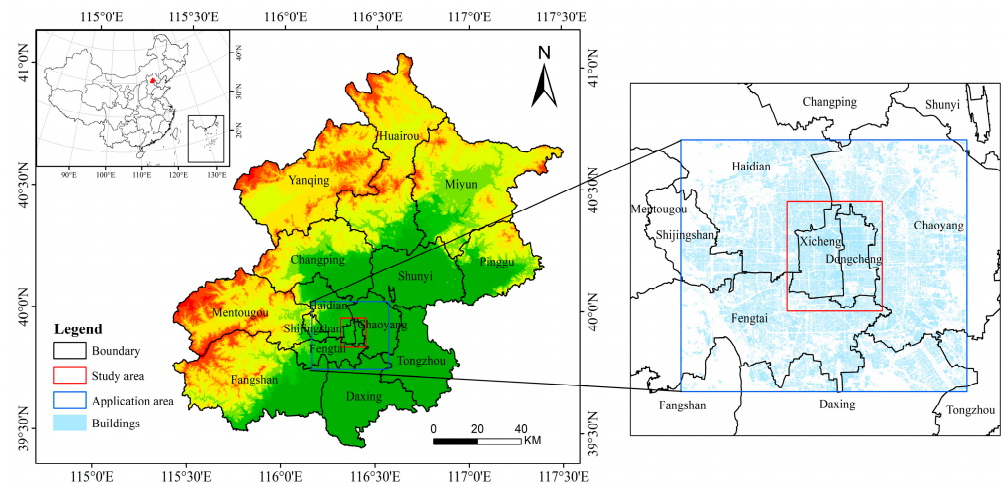


Figure 1. The study area of Beijing, China.

3.2. Data Source

Three types of data are used in this study: building function type data, Sentinel-2 remote sensing data, and mobile signaling data.

3.2.1. Building Function Type Data

The building function type data used in this study are acquired from OSM (<https://www.openstreetmap.org/#map=4/36.81/102.83> (accessed on 27 December 2020)), Data Sharing (DS) (<https://data.yunshudu.com/detail.html?id=10051> (accessed on 27 December 2020)), and Gaode Map (<https://ditu.amap.com/> (accessed on 27 December 2020)). OSM is an open-source map provider that aims to provide users free and easily accessible digital map resources [51] and is considered to be the most successful and prevailing Volunteered Geographic Information (VGI) at this time [52]. It contains a wide variety of thematic layers, such as building footprints, land use, railways, roads, water, traffic, and transport. In regard to BFT identification, the positions and shapes of buildings are necessary. Thus, the building footprint of OSM was chosen as the base data source in this study. In addition to the building geometric features of the footprint polygon, the building function tags (name, type) were also used and taken as the training and test references in the RF model construction.

Note that as the OSM data are produced by volunteers, some buildings are not included in the OSM building footprint layer or the BFT is mislabeled. Thus, DS data were used to fill the building footprint polygons, as the corresponding buildings in the original OSM had been overlooked. Then, the street view of Gaode Map was used to fill in the buildings' function tag, as the corresponding building labels in the original OSM were not available. The OSM BFT tags were subsequently checked using Gaode Map to ensure that no buildings were mislabeled. As the MS data had been acquired in 2020, the OSM data and its supplementary data from 2020 were used to accompany the MS data.

3.2.2. Mobile Signaling Data

The MS data used in this study were produced by a third-party push service provider of GeTui Company (<https://www.getui.com/> (accessed on 25 December 2020)) that offers Android and iOS push Software Development Kit (SDK) services. Due to the SDK embedded in the users' mobile devices to dynamically collect relevant device location information at certain time intervals based on real-time locations reported by the mobile devices, the population at a given location can be sampled and acquired [37]. According to the 2020 Annual Report released by GeTui, the cumulative number of SDK installations exceeded 68 billion, with over 400 million daily active unique devices. This certainly provides a valid dataset for large-scale population dynamics studies.

Before further data processing and analysis, the coarse MS data were preprocessed by GeTui and stored in Geohash format. When retrieving data based on addresses, Geohash is

the usual method for the repository of very large amounts of spatial data, which divides the entire geospace into rectangular squares (grids) of different levels. The two-dimensional latitude and longitude are converted into strings in Geohash format with different lengths, each of which represents a certain geo-grid. All the objects within the same grid share the same Geohash locational string. The longer the string is, the higher the locational accuracy of the range represented. GeoHash6, GeoHash7, and GeoHash8 indicate that the locational strings are represented using six, seven, and eight characters or numbers, respectively, such as "wx41e", "ws07pr0", and "ws07pr0m". The spatial resolutions of GeoHash6, GeoHash7, and GeoHash8 are approximately $1.2 \text{ km} \times 0.6 \text{ km}$ (in the longitude and latitude directions, respectively), $150 \text{ m} \times 150 \text{ m}$, and $30 \text{ m} \times 20 \text{ m}$, respectively. As the Geohash grid size is as large as the kilometer scale (Geohash6), it may contain buildings with a variety of functional types, namely, mixed grids of functional types. As the grid is too fine in meters (Geohash8), a building may be split into different Geohash grids. In addition, fine grids may include too few samples to study the characteristics of diurnal dynamic variations. Thus, the MS data in GeoHash7 with a resolution of hundreds of meters were considered and used in this study. The Geohash7 grids are shown in Figure 2, and each grid represents a rectangular area of $150 \text{ m} \times 150 \text{ m}$. Assuming that the rectangular area is homogeneous in BFTs, the corresponding BFTs can be estimated based on the method proposed in this study.

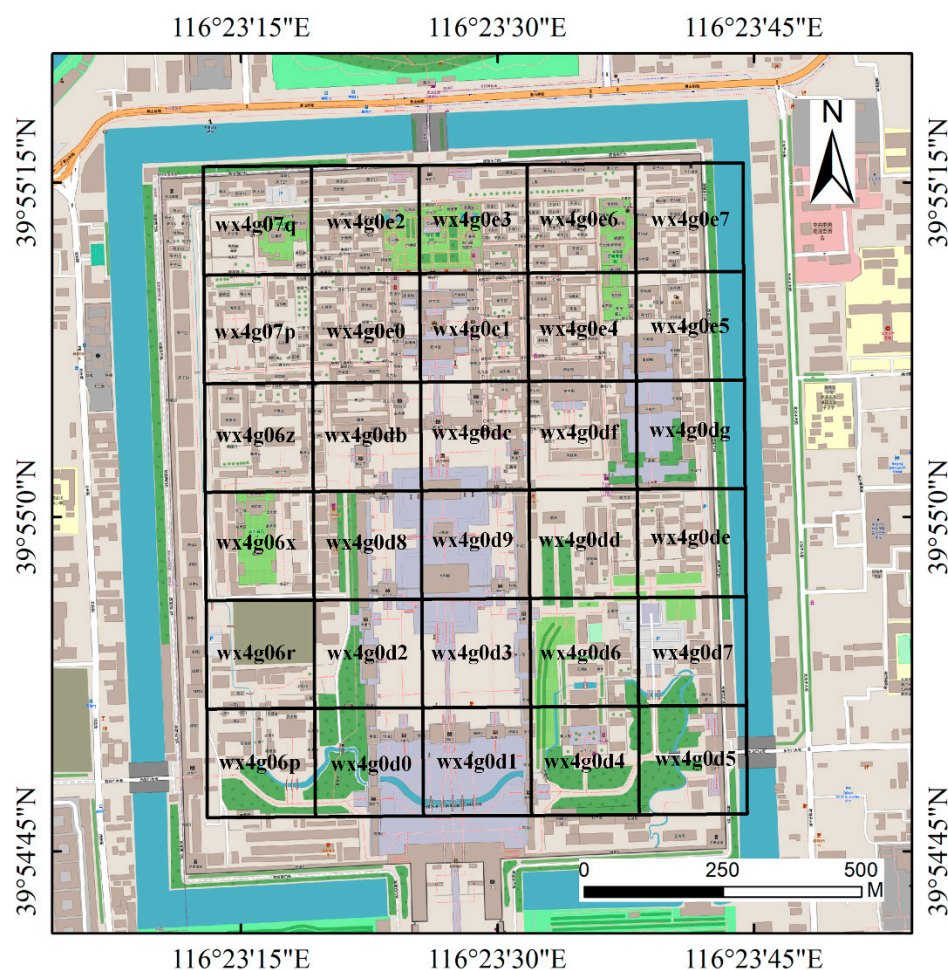


Figure 2. Example of Geohash7 grids in the central parts of the study area.

Note that the mobile devices were sampled through the embedded SDK, namely, not all the devices were acquired and reported for a given moment within the given Geohash grid (generally at a low sample rate to save mobile device power under normal conditions). To improve the sample rates, the MS data were accumulated at an interval of an hour. Thus, the same devices may have been sampled more than once at the same Geohash

grid or sampled at different grids during the one-hour time range. To reduce duplicate samples, data cleaning was performed. As the data reported by SDK included some private information, such as phone numbers, after data cleaning, the data were anonymous and could be delivered to the users. The MS data were accumulated over an hour because the BFT was estimated based on the diurnal variation in the MS data. If the temporal resolution was too coarse, the variation differences between different BFTs could not be detected by means of MS data.

Considering the obvious differences in human dynamics between weekdays and weekends, two days of MS data from the study area in Beijing in 2020 were collected: 9 December 2020 (Wednesday) and 12 December 2020 (Saturday). Four types of MS indicators were provided by GeTui and used in this study:

(1) Station

Station represents the number of active communication base stations that can be scanned by the mobile devices in each Geohash grid per hour. Mobile devices regularly report information on scanned base stations, and base stations within a specified geographical area are acquired based on the base station beacon location database.

(2) Gid

Gid stands for the number of online mobile devices in each Geohash grid per hour connected through active communication base stations. The mobile device location (Geohash grid) is calculated based on multiple location methods with the active communication base stations' locations.

(3) Wifimac

Wifimac is the number of active Wi-Fi hotspots in each Geohash grid per hour. Mobile devices report the scanned active Wi-Fi hotspot information at regular intervals, and the Wi-Fi hotspots within a specified geographic area can be acquired based on the Wi-Fi beacon location library.

(4) Loginmac

Loginmac is the number of Wi-Fi-connected mobile devices in each Geohash grid per hour. Based on the last indicator of the active Wi-Fi hotspots within a given Geohash grid, we can obtain the corresponding connected mobile devices.

The MS data acquired from the third-party push service provider were saved in txt format, with the corresponding fields of "data acquisition time, Geohash Grid String, Station, Gid, Wifimac, Loginmac".

3.2.3. Sentinel-2 Data

The S2 images were downloaded through the European Space Agency (ESA) Application Programming Interface (API) Hub (<https://scihub.copernicus.eu/> (accessed on 24 January 2022)). Sentinel-2 is a high-resolution multispectral imaging satellite launched by the ESA. It is a binary satellite system of Sentinel-2A and Sentinel-2B with an orbit interval of 180°. The revisit period of one satellite is 10 days, and the revisit period is reduced to 5 days when the two satellites are synchronized in operation. With an orbit altitude of 786 km above ground and a field of view of 20.6°, S2 has a coverage width of 290 km at the ground. As Table 1 shows, S2 has 13 spectral bands from visible to shortwave infrared wavelengths with three different ground spatial resolutions of 10 m, 20 m, and 60 m (under vertical view conditions).

Table 1. S2 band attributes.

Sentinel-2 Bands	Central Wavelength (nm)	Bandwidth (nm)	Spatial Resolution (m)
Band 1—Coastal aerosol	443	20	60
Band 2—Blue	490	65	10
Band 3—Green	560	35	10
Band 4—Red	665	30	10
Band 5—Vegetation Red Edge	705	15	20
Band 6—Vegetation Red Edge	740	15	20
Band 7—Vegetation Red Edge	783	20	20
Band 8—NIR	842	115	10
Band 8A—Vegetation Red Edge	865	20	20
Band 9—Water vapour	945	20	60
Band 10—SWIR—Cirrus	1375	30	60
Band 11—SWIR	1610	90	20
Band 12—SWIR	2190	180	20

To reduce the influence of clouds and cloud shadows, good quality S2 images of the study area with cloud coverage less than 5% were selected. Finally, two S2 images from 21 June 2020 and 8 December 2020, with file names L1C_T50TMK_A026098_20200621T031232 and L1C_T50TMK_A028529_20201208T031118 were used in this study.

4. Method

4.1. Definition of Building Function Types

In sophisticated classification schemes, for practical applications, BFTs are highly overlapping and not well defined, which makes classification using machine learning extremely difficult [17]. As shown in Table 2, many studies have focused on BFT classification with different classification schemes. Based on previous studies and driven by the diurnal variation patterns of the population dynamics within different building types, we propose a BFT classification scheme with five categories: residential (*R*), working (*W*), entertainment (*E*), visiting (*V*), and hospital (*H*). This classification is useful for urban management and disaster emergency response, which are oriented to population dynamics, because urban management science and disaster emergency response are closely related to the spatial and temporal distribution and dynamic changes in sociodemographic parameters.

Table 2. Building function type classification schemes used in past studies.

Authors	Function Types
[2]	Residential, urban villages, office, shopping centers, hotels, hospitals, schools
[3]	The mixed type of office, residential, recreation, shopping
[4]	Residential, commercial, office, warehouse, public service, mixed-function
[17]	Commercial, residential, public, industrial
[24]	Hospital, hotel, office, residence, restaurant, retail, school

According to our classification framework, the definition of each BFT is as follows:

- (1) *R* represents buildings holding residential properties, such as houses, apartments, and student dormitories. Generally, residents wake up in the morning, move to other functional buildings based on their daily activities from approximately 7:00 to 9:00 a.m., and return to their own residences from approximately 18:00 to 19:00 p.m. There are relatively few people in residential areas during working hours. Thus, on the one hand, the population dynamics in the BFT of *R*-type buildings generally show an obvious diurnal variation on working days. The population dynamics on weekends, on the other hand, generally show a gentler variation with respect to those on weekdays.

- (2) *W* represents working or studying places, such as commercial/government office buildings and teaching buildings. *W*-type buildings are more densely populated during the daytime on weekdays and sparsely populated during the evening and on weekends.
- (3) *E* stands for buildings used for entertainment. As compared with *W*-type buildings, *E*-type buildings commonly have relatively longer and optional opening hours each day and later opening and closing times. These buildings include shopping malls, cinemas, bars, and restaurants. The corresponding time of the population peak in *E*-type buildings is later than that in *W*-type buildings. Different from *W*, *E* have more people on weekends than on weekdays.
- (4) *V* is a group of recreational buildings of a visiting or educational nature, such as tourist attractions, museums, and art galleries. Different from *E*-type buildings, *V*-type buildings generally have fixed opening hours and do not open during the night. *V*-type buildings have a similar character to *W*-type buildings during weekdays. Similar to *E*, *V*-type buildings are more densely populated on weekends than on weekdays.
- (5) *H* stands for the collection of buildings with a medical nature, such as hospitals and clinics. These buildings have some similarities with *W*-type buildings. The population is denser during the daytime on weekdays and sparser on weekday evenings and on weekends. However, there is a special pattern in which the maximum population occurs from 8:00 a.m. to 10:00 a.m. and drops substantially after 10:00 a.m. This is because people tend to arrive at the hospital earlier in the day.

4.2. Data Processing

4.2.1. Reference Data Construction

To construct the RF model, the data from OSM are selected as the references for the model training and testing. Note that the OSM data contain many building function categories, far more than the five categories defined in Section 4.1. Thus, all the buildings with valid BFT tags in OSM were reorganized into the five groups, as shown in Table 3.

Table 3. Building function types and the corresponding OSM and Gaode classes.

Function Type	OSM Types	Supplemented by Gaode
Residential (<i>R</i>)	Residential, apartments, dormitory, hotel, house	College/university dormitory
Working (<i>W</i>)	Office, company, industrial, school, kindergarten, warehouse	Bank, financial center, office, Factory, teaching building
Entertainment (<i>E</i>)	Retail	Shopping mall, cinema, bar
Visiting (<i>V</i>)	Church, parking, place of interest	museum, gallery
Hospital (<i>H</i>)	Hospital	Clinic, medical treatment

Notably, not all the buildings have BFT values in the OSM data, namely, some of the buildings' BFT tags are empty. To increase the sample size, the street view of Gaode Map was used to identify building types when they were not available in the original OSM data. For buildings with mixed functions, the dominant type was used and assigned to the corresponding buildings. For example, some multistory residential buildings had a first floor that was used as a restaurant or for retail, and they were taken as *R*-type buildings, as most of the floors had a residential function.

The MS data used in this study were in Geohash format with a spatial resolution of 150 m × 150 m. To accompany the MS data, the BFT data in vector format were converted into raster format with a spatial resolution of 150 m × 150 m. For mixed pixels containing more than one type of building, the dominant type accounting for the greatest proportion with respect to area was assigned to the corresponding pixel. Figure 3 shows some examples of data format conversion from vector to raster. Then, 750 rasterized samples comprising 291 *R* samples, 168 *W* samples, 70 *E* samples, 174 *V* samples, and 47 *H* samples were finally obtained. Figure 4a shows the sample data in vector format, and Figure 4b shows the converted samples in raster format with a spatial resolution of 150 m × 150 m. The building samples with different BFTs are shown in Figure 4 in different colors. It can be seen that the

samples data only account for approximately 11% of the study area. The BFTs of the rest of the study area were estimated using the model proposed in this study.

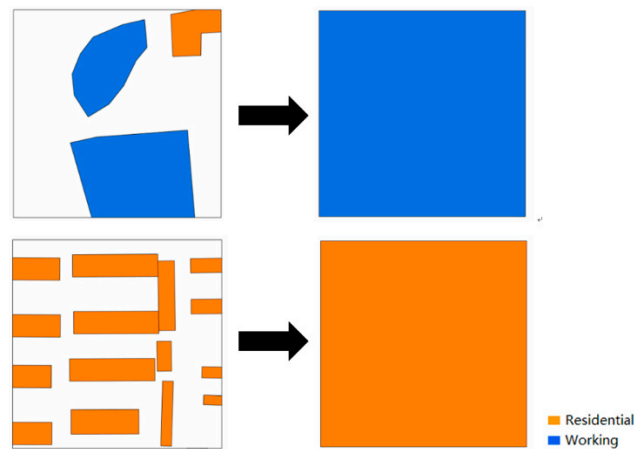


Figure 3. Examples of standard grid function definitions.

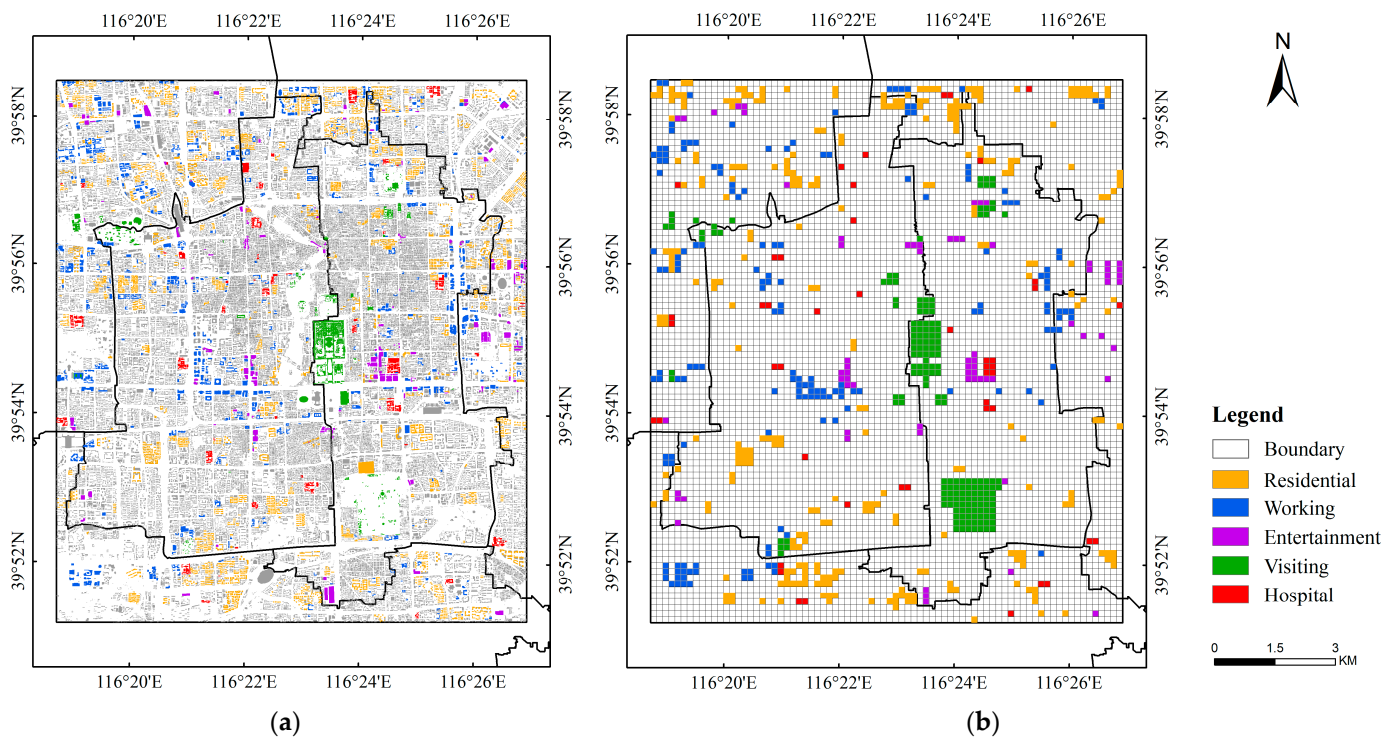


Figure 4. The distribution of building function type (BFT) samples used in this study according to OSM and Gaode classes: (a) Building level in vector format; (b) pixel level in raster format.

4.2.2. Mobile Signaling Data

Due to the differences in population spatial distributions and buildings' population capacities (mainly the number of buildings' floors), the absolute values of MS data within different grids show a considerable difference. Since our focus was on analyzing and using the differences in the diurnal variations of MS data for different BFTs, to reduce the influence of the substantial difference in the absolute values in the MS data, the 48 MS data for each sample (24 h of weekday data and 24 h of weekend data) were normalized via the Z score method, which is commonly used in classification and clustering algorithms. The MS data after normalization conformed to the standard normal distribution with a

mean of 0 and a standard deviation of 1. The normalization of the original absolute values (after spatial resampling) of grid(i,j) is calculated as:

$$Zscore_{ij}(t) = \frac{X_{ij}^{abs}(t) - \mu_{X_{ij}^{abs}}}{\sigma_{X_{ij}^{abs}}} \quad (1)$$

where $X_{ij}^{abs}(t)$ and $Zscore_{ij}(t)$ represent the original and normalized MS values of grid(i,j) at moment t and i and j are the coordinate values in the longitude and latitude directions, respectively; $\mu_{X_{ij}^{abs}}$ is the mean of grid(i,j) over 48 h; $\sigma_{X_{ij}^{abs}}$ is the standard deviation of grid(i,j) over 48 h.

As there were four different types of MS indicators, four sets of $Zscore_{ij}(t)$ values were calculated. Figure 5 shows the 48-hour time series of the four indicators for each of the five BFTs obtained by averaging the Z score values of all samples contained in each BFT at moment t (t is from 1 to 24 for the weekday and 25–28 for the weekend). As shown in Figure 5, because the MS data obtained in this study have a temporal resolution of one hour, the plotted curves are not smooth, but it is not difficult to observe that each category shows different dynamic patterns.

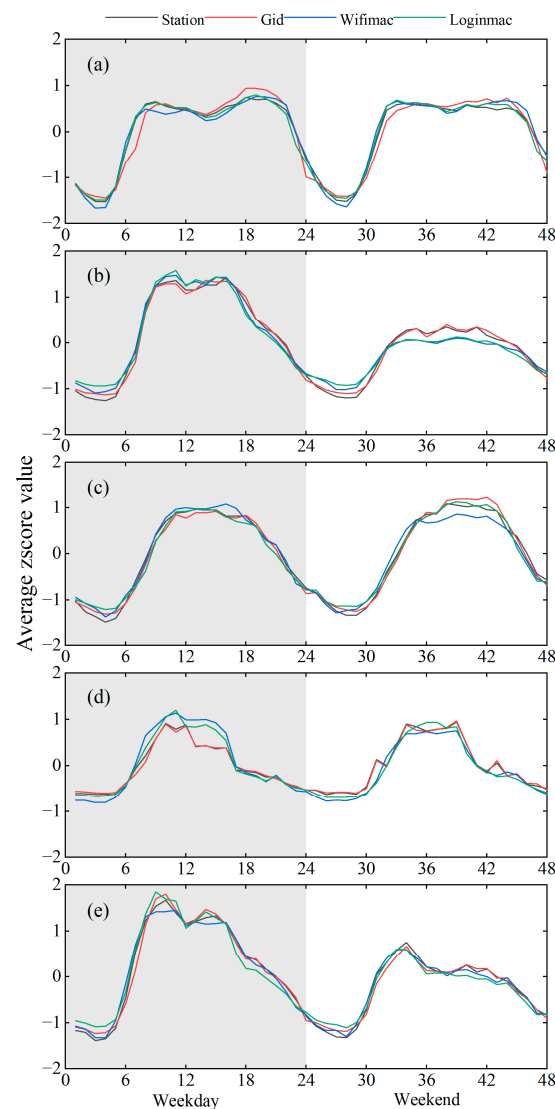


Figure 5. Average value of four MS indicators after normalization for each of the five BFTs: (a) Residential; (b) working; (c) entertainment; (d) visiting; (e) hospital.

- (1) Figure 5a shows that *R*-type buildings have higher MS activity in the early morning hours and late at night on weekdays, and the peaks occur between 7:00 and 9:00 a.m. and 18:00 and 21:00 p.m. On the weekend, MS activity shows a more moderate variation.
- (2) In Figure 5b, *W*-type buildings have higher MS activity between 9:00 a.m. and 17:00 p.m. on weekdays and generally have a short period at approximately 12:00 a.m. (lunch time). As compared with weekdays, MS activity within *W*-type buildings is significantly lower on the weekend.
- (3) In Figure 5c, MS activity in *E*-type buildings is concentrated between 10:00 a.m. and 18:00 p.m. on weekdays, while the MS data peak plateau tends to be delayed to between 12:00 p.m. and 22:00 p.m. on the weekend, and there is more MS activity on the weekend than on weekdays.
- (4) In Figure 5d, MS activity within *V*-type buildings is concentrated between 9:00 a.m. and 16:00 p.m. on both weekdays and weekends, the difference being that there is more activity on weekends.
- (5) Figure 5e shows that MS activity in *H*-type buildings is greater during weekdays and sparser on weekends and weekday evenings. In addition, there is a special peak period between 8:00 a.m. and 10:00 a.m. on both weekdays and weekends.

These time-series changes in MS data indicate a relationship between MS activity and BFT. Mobile devices can be used as sensors of people's activities to recognize people's time-series change patterns within buildings to distinguish different BFTs.

4.2.3. Sentinel-2 Data

(1) Image preprocessing

The downloaded Sentinel-2 data are L1C-level top-of-atmosphere (TOA) reflectance products after orthorectification and geometric correction, without radiometric calibration and atmospheric correction. To obtain valid S2 images of the study area, atmospheric correction, resampling, clipping, and cloud masking are necessary. Figure 6 shows the preprocessing flow of S2 images.

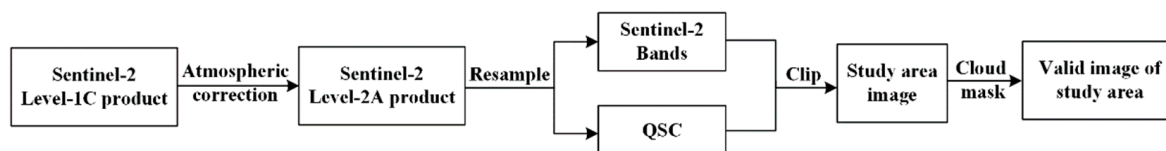


Figure 6. The preprocessing flow of Sentinel-2 data.

First, the open-source Sen2cor plug-in provided by ESA was used to perform atmospheric correction of S2 images to obtain L2A-level products. After atmospheric correction, the bottom-of-atmosphere (BOA) reflectance can be acquired from the TOA reflectance. Second, the S2 images with spatial resolutions of 20 m and 60 m were resampled to 10 m with the open-source software Sentinel Application Platform provided by ESA. Third, to match the study area and reduce image volumes, the S2 images of the study area were masked based on the images after resampling. Note that space-borne optical images are inevitably affected by clouds and cloud shadows [53,54]. The final process was cloud masking according to the quality scene classification, a quality control file produced after Sen2Cor atmospheric correction. After these steps, we obtained 10 m resolution images of the study area for subsequent feature extraction.

(2) Feature extraction

The target of BFT classification in this study is different from the traditional land use or land cover classification. The same building can be used for residents or working, which is difficult to distinguish based on remote sensing images. However, the land cover or land use types can be clearly detected by spaceborne or airborne remote sensing images.

To improve the classification accuracy, the widely used spectral and texture features were both used in this study for S2 image-based BFT classification.

The spectral features used in this study include the BOA surface reflectance of individual bands after preprocessing and six spectral indices. Since B10 is designed for cirrus detection and has a low atmospheric transmittance with nearly no ground information, the remaining 12 bands, in addition to B10, were considered in this study. Because the MS data used in this study had a spatial resolution of 150 m, the S2 bands were resampled to 150 m. As compared with the 12-band BOA reflectance, the spectral indices calculated based on some band combinations could enhance the ground features of interest and reduce the influence of the atmosphere [55]. Two types of spectral indices were considered: normalized indices and principal component transformed indices. The normalized difference built-up index (NDBI), modified normalized difference water index (MNDWI), and normalized difference vegetation index (NDVI) were selected as normalized indices, and the tasseled cap brightness (TCB), tasseled cap greenness (TCG), and tasseled cap wetness (TCW) obtained from the tasseled cap transformation (TCT) were selected as principal component transform indices, whose formulas are shown in Table 4. With 12 bands' BOA surface reflectance and six spectral indices in Table 4, this process generates a total of 36 spectral features for the winter and summer S2 images.

Table 4. Name and calculation formula of spectral indices used in this article.

Name	Calculation formula
Normalized difference built-up index	$NDBI = (B11 - B8)/(B11 + B8)$
Modified normalized difference water index	$MNDWI = (B3 - B11)/(B3 + B11)$
Normalized difference vegetation index	$NDVI = (B8 - B4)/(B8 + B4)$
Tasseled cap brightness	$TCB = 0.3510 \cdot B2 + 0.3813 \cdot B3 + 0.3437 \cdot B4 + 0.7196 \cdot B8 + 0.2396 \cdot B11 + 0.1949 \cdot B12$
Tasseled cap greenness	$TCG = -0.3599 \cdot B2 - 0.3533 \cdot B3 - 0.4737 \cdot B4 + 0.6633 \cdot B8 + 0.0087 \cdot B11 - 0.2856 \cdot B12$
Tasseled cap wetness	$TCW = 0.2578 \cdot B2 + 0.2305 \cdot B3 + 0.0883 \cdot B4 + 0.1071 \cdot B8 - 0.7611 \cdot B11 - 0.5308 \cdot B12$

As discussed previously, remote sensing-based BFT classification is difficult when using only spectral information at the pixel scale, especially the commonly used vertical viewing satellite images, which can only obtain information about building roofs. Buildings with the same roof material (with the same reflectance) can be used for living, office, and even industry space. As the same functional buildings commonly have similar characteristics with respect to dimensions and spatial distributions and are generally grouped together in space and shown as certain texture characters in the dimension of direction, grayscale difference, and interval in remote sensing images, the texture features were also used in this study.

Texture in remote sensing describes the spatial variation of the light intensity reflected by the observation target [20]. The use of texture metrics associated with classification algorithms in medium- and high-resolution image classification can significantly improve the OA of image classification, especially for urban areas [56–59]. In 1973, Haralick proposed the gray-level co-occurrence matrix (GLCM) to describe texture features by studying the spatial correlation of grayscale [60]. GLCM has since been widely used for remote sensing studies of regression or classification. Thus, the texture features of the GLCM were also used for BFT classification. Eight GLCM metrics were considered, namely, mean, variance, homogeneity, contrast, dissimilarity, entropy, second moment, and correlation [61]. The details of the metrics are shown in Table 5.

Table 5. Name and calculation formula of the GLCM texture features used in this study.

Texture Feature	Calculation Formula
Mean	$\sum_{i=0}^{N-1} \sum_{j=0}^{N-1} i \times p(i, j)$
Variance	$\sum_{i=0}^{N-1} \sum_{j=0}^{N-1} (i - u)^2 p(i, j)$
Homogeneity	$\sum_{i=0}^{N-1} \sum_{j=0}^{N-1} \frac{1}{1+(i-j)^2} p(i, j)$
Contrast	$\sum_{i=0}^{N-1} \sum_{j=0}^{N-1} (i - j)^2 p^2(i, j)$
Dissimilarity	$\sum_{i=0}^{N-1} \sum_{j=0}^{N-1} p(i, j) i - j $
Entropy	$\sum_{i=0}^{N-1} \sum_{j=0}^{N-1} p^2(i, j) \ln(p(i, j))$
Second Moment	$\sum_{i=0}^{N-1} \sum_{j=0}^{N-1} p(i, j)^2$
Correlation	$\frac{\sum_{i=0}^{N-1} \sum_{j=0}^{N-1} ij p(i, j) - \mu_x \mu_y}{\sigma_x \sigma_y}$

The GLCM reflects the comprehensive image grayscale information about adjacent intervals, change magnitudes, and directions. Thus, the choice of sliding window size and direction has a considerable impact on the performance of the texture analysis of the GLCM. Since the resolution of the MS data was 150 m, the image pixels within the 150 m box were used to extract texture features. Namely, the window size was 15 for all 10 m resolution image layers after resampling. For directions, RF models between texture features and real BFT under four directions (0°, 45°, 90°, and 135°) were established with the same data, and the GLCM features had a better performance in the 90° direction. To adapt to the resolution of the MS data, the calculated texture features of the S2 images were resampled to 150 m. With eight GLCM metrics for each of the 12 bands, this process generated a total of 192 (12 bands × 8 metrics × 2 images) variables for the winter and summer S2 images.

4.3. Random Forest Model

4.3.1. Parameter Setting

The RF model is a combinatorial classifier of decision trees. As shown in Figure 7, it uses bootstrap random resampling to draw multiple samples from the original dataset, models a decision tree for each bootstrap sample, and then combines these decision trees to obtain the final classification results by voting. In addition, a subset of all the features is randomly selected for each decision tree. Thus, for each decision tree, the training samples and features used may be different. By training on different parts of the same training set and different parts of features for individual decision trees, the RF model reduces the effects of overfitting and improves generalization. Because of its high tolerance for outliers and noise, the RF model was selected for BFT classification in this study. The main factors affecting its classification accuracy and efficiency included the parameter settings and feature selection. Therefore, we focused on these factors to optimize the model and to improve the performance of the classifier.

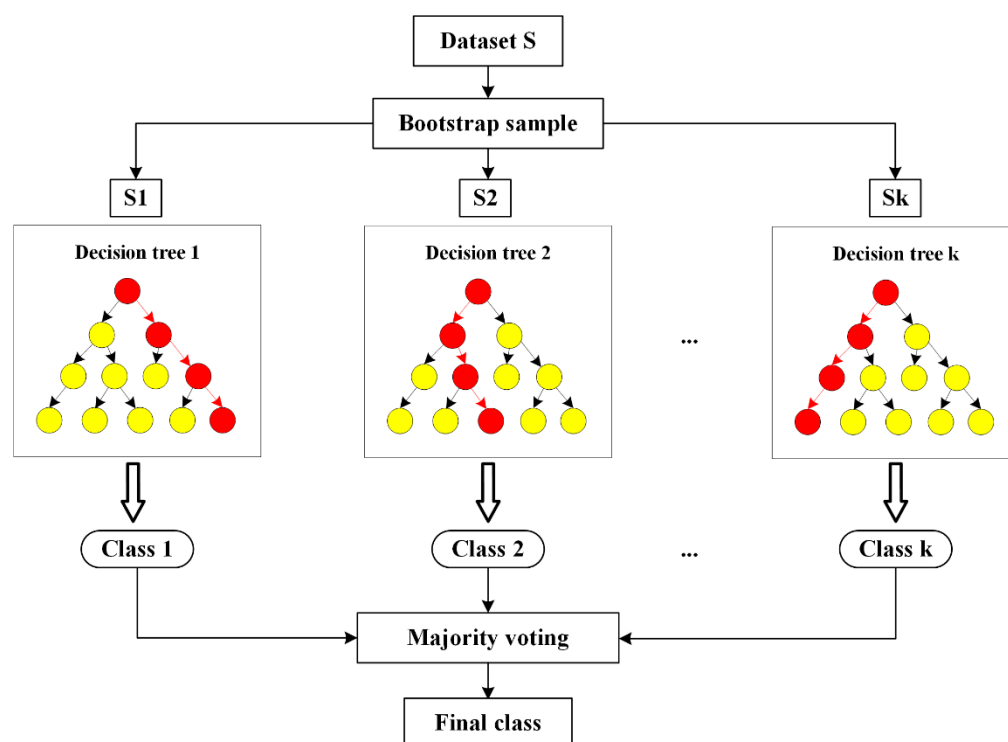


Figure 7. Illustration of the random forest classification model.

(1) Parameter setting

The number of decision trees (N) and leaves (L) are two major parameters that influence the classification accuracy of the RF model. Breiman demonstrated that the generalization error of the model gradually started to converge as N increased [62]. However, experimental evidence has shown that it was not the case that the larger the N was, the better the classification accuracy [63]. To acquire the optimal parameter combination for BFT classification, N was increased from 50 to 1000 in steps of 50 in RF model construction, while L values of 1, 5, 10, 20, 50, and 100 were considered for individual N conditions. Then, the corresponding N and L were selected according to the out-of-bag (OOB) classification accuracy.

(2) Feature selection

Figure 5 shows that the four MS indicators are similar to each other. The BFT classification performance of each indicator must be evaluated independently to select the optimal indicator. Then, the time-series features (48 indices for weekdays and weekends) of the optimal indicator are selected to construct the RF model. In practical classification applications, the number of features that can be selected is usually more than the number needed. If all these features are selected without any consequences, not only will it not help the classification effect but also the classification accuracy will be degraded and the classification time will be too long due to the “Hughes phenomenon” [64]. Feature optimization can effectively improve classification efficiency and reduce elapsed time while ensuring classification accuracy [65].

This study used a combination of qualitative and quantitative analysis to select one of the four indicators. The qualitative analysis compared the corresponding ability to demonstrate diurnal population dynamics. The samples selected in the previous step were first classified into the five BFTs defined in Section 4.1; then, the Zscore mean values of the 48-h time series of each BFT sample were calculated and plotted. Next, the Z score mean values of the indicator most consistent with the assumed diurnal population dynamics were selected. The quantitative analysis compared the BFT classification accuracy of the four indicators. After constructing the RF model with each of the four indicators separately, the OOB accuracy of each model was compared to select the final indicator used in this study.

Once the MS indicator was determined, feature selection must also be considered. Feature selection included the following main steps. First, the feature importance of MS data is calculated in the RF model. Then, the features are ranked in terms of importance in descending order. Second, the RF model is constructed with different input features according to the feature importance ranking, namely, using the first feature with the highest importance at the first time, selecting the first two features the second time, and so on. The RF models' OOB classification accuracy of different feature combinations is then calculated. Finally, the feature combination with the largest OOB classification accuracy is taken as the final feature combination for BFT classification. S2 features are selected in the same way.

4.3.2. RF Model Construction

After selecting the optimal MS indicator and combining weekday and weekend time-series features, the proposed mobile signaling random forest classification model (MS-RF) was constructed to predict the BFTs of the study area. For comparison, another RF model, a Sentinel-2 random forest classification model (S2-RF) was also constructed based on the 12 spectral bands of S2 images, six spectral indices, and 8 texture features of each band.

To construct the RF models, the cross-validation method was used with 70% of the 750 randomly selected samples as training data and the remaining 30% as test data. To provide a relatively stable result, this process was repeated ten times, and the mean and standard deviation of the classification accuracy were calculated. The flow chart is shown in Figure 8.

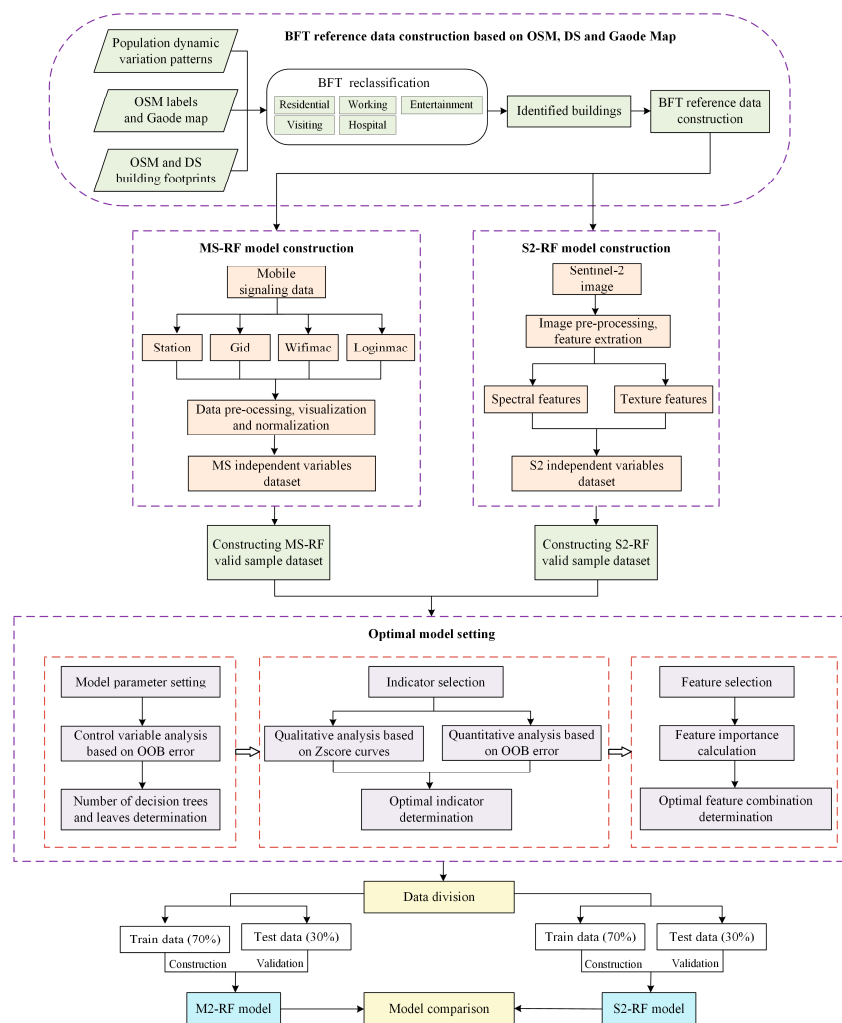


Figure 8. Construction process of the MS-RF and S2-RF models.

5. Results

5.1. Classification Results of Different Model Settings

5.1.1. Classification Accuracy with Different Numbers of Trees and Leaves

The numbers of decision trees and leaves have significant influences on the classification accuracy of the RF model. Figure 9a–d show the OOB classification accuracy of four MS indicators, i.e., Station, Gid, Wifimac, and Loginmac, with respect to the number of trees for different leaves. For all four indicators, the OOB classification accuracy tends to increase as N increases, and when N is greater than 500, the accuracy tends to be stable; however, the training time increases substantially. In addition, as shown in Figure 9, when L is 1, the corresponding OOB accuracies are all the highest in Figure 9a–d. Therefore, an N of 500 and an L of 1 are selected as the final parameters for RF model construction.

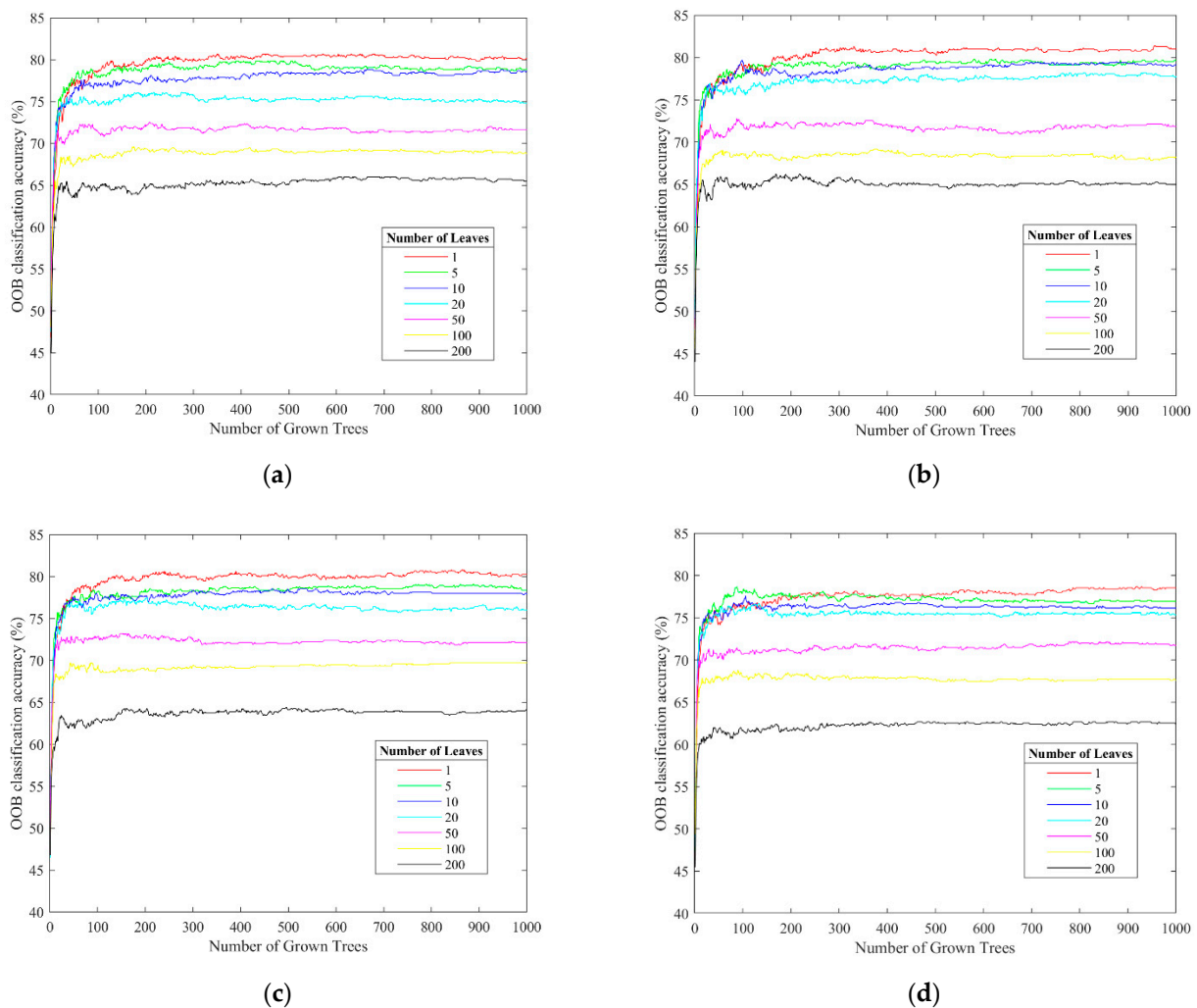


Figure 9. OOB classification accuracy for the four MS indicators with different numbers of trees and leaves: (a) Station; (b) Gid; (c) Wifimac; (d) Loginmac.

5.1.2. MS Indicator Selection Results

The four MS indicators were evaluated according to the qualitative and quantitative analysis methods proposed in Section 4.3.1. Regarding the qualitative results, as shown in Figure 5a,b, all four indicators show similar trends and are in accordance with the assumed population dynamics patterns in the R and W BFTs. Namely, people within R -type buildings usually show a strong pattern of variation during the working day, more activity in the morning or evening, and less during the daytime working hours. Conversely, W -type buildings typically have more activity during working hours on weekdays and fewer in the

mornings, evenings, and on weekends. Therefore, all four indicators are effective for the discrimination of *R* and *W*. For BFT *E* in Figure 5c, the curves of the three indicators Station, Gid, and Loginmac show the expected pattern, while Wifimac is lower on weekends than on weekdays. This is not in accordance with the general human dynamics pattern, indicating that the performance of Wifimac in discriminating *E* is relatively poor. For BFT *V* in Figure 5d, both Wifimac and Loginmac show an overall tendency of having fewer activities on weekends than weekdays. This is not consistent with the expected pattern, namely, people tend to go to places such as museums on weekdays. For *H* in Figure 5e, all four indicators show reasonable regularity. In summary, the results based on the qualitative analysis indicate that Station and Gid perform best in distinguishing the five BFTs.

To further obtain the optimal MS indicator for classification, the quantitative results must be combined. Four different RF models are constructed with the input features of the four individual MS indicators. Figure 10 shows the corresponding OOB classification accuracy of the five BFTs for the four MS indicators. The overall OOB and all five BFT classification accuracies of the RF model built with Gid are larger than those of the others. Therefore, we take Gid as the optimal indicator for further study.

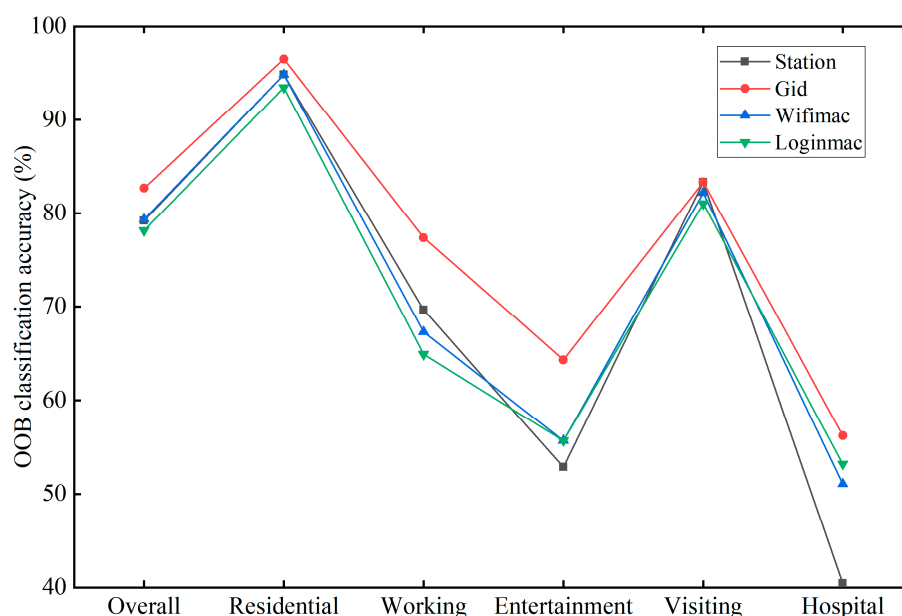


Figure 10. OOB classification accuracy of the five building function types for the four MS indicators.

5.1.3. Feature Selection Results

The importance ranking of the input features of the MS-RF model is calculated and shown in Figure 11, with the features from weekdays and weekends shown in gray and white background colors, respectively. With the input features in descending order with respect to the corresponding importance, the corresponding OOB classification accuracies of the MS-RF model can be calculated. The classification accuracies of the MS-RF model with respect to different numbers of input features are shown in Figure 12.

For the MS-RF model shown in Figure 12, the combination of the first 23 features (ranked in descending order with respect to importance) has the largest OOB classification accuracy. Thus, the MS features whose importance ranks between the 24th and 48th are discarded. The selected features are given in orange, and unselected features are shown in blue in Figure 11. According to the importance ranking shown in Figure 11, the MS features on weekdays (shown on a gray background) have a higher importance in the BFT classification as compared with those on weekends (shown on a white background). More weekday input features than weekend input features are used in MS-RF construction, with 16 input features from weekdays and seven input features from weekends, because the

classification frame proposed in Section 4.1 relies more on the variations in population dynamics on weekdays.

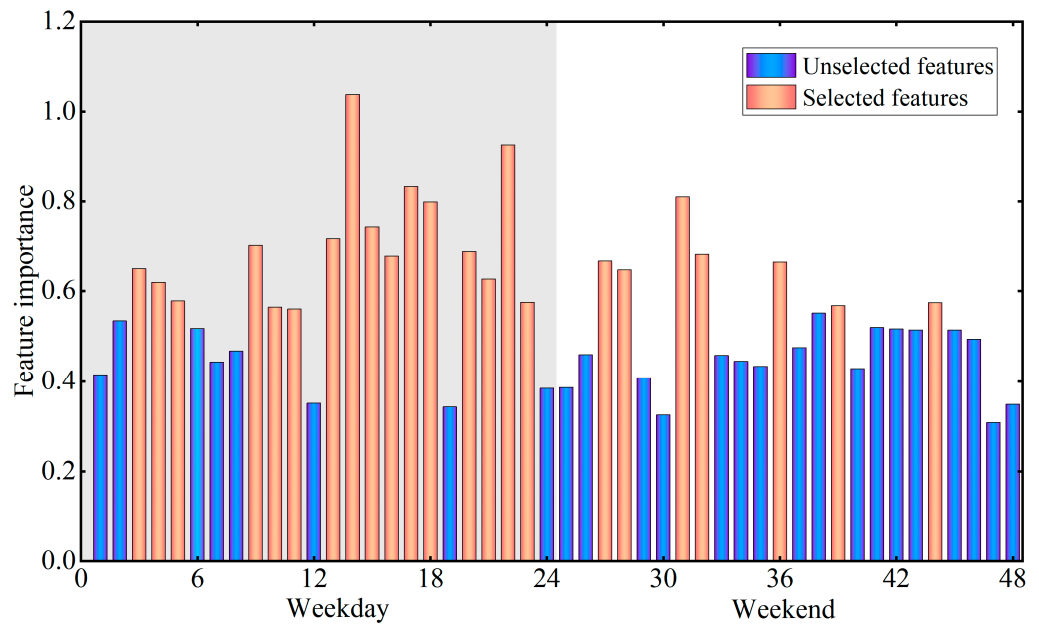


Figure 11. Importance ranking of MS input features.

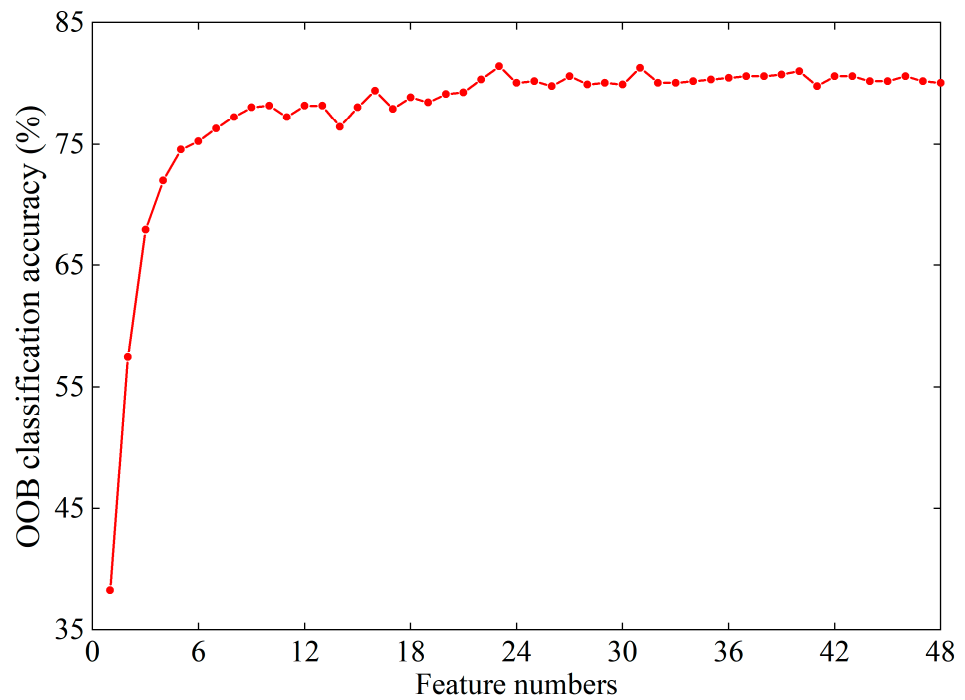


Figure 12. RF OOB classification accuracy with different numbers of MS features.

Similarly, importance ranking of the input features of the S2-RF model is calculated and shown in Figure 13, with the features from 21 June 2020 to 8 December 2020 shown in gray and white background colors, respectively. In addition, the spectral and texture features of the S2 images used in this study are also labeled in Figure 13. The classification accuracies of the S2-RF model with respect to different numbers of input features are shown in Figure 14, with the input features ranked in descending order of feature importance.

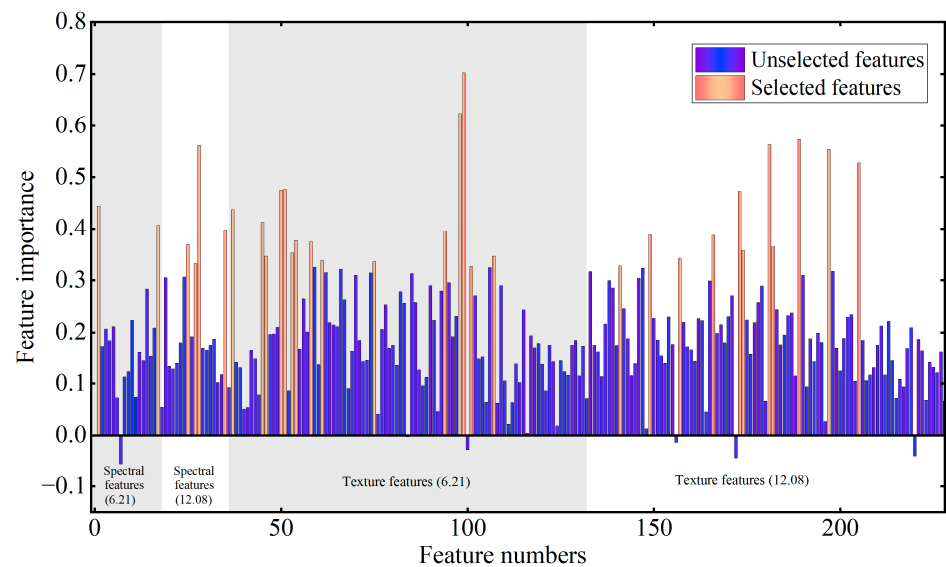


Figure 13. Importance ranking of S2 features.

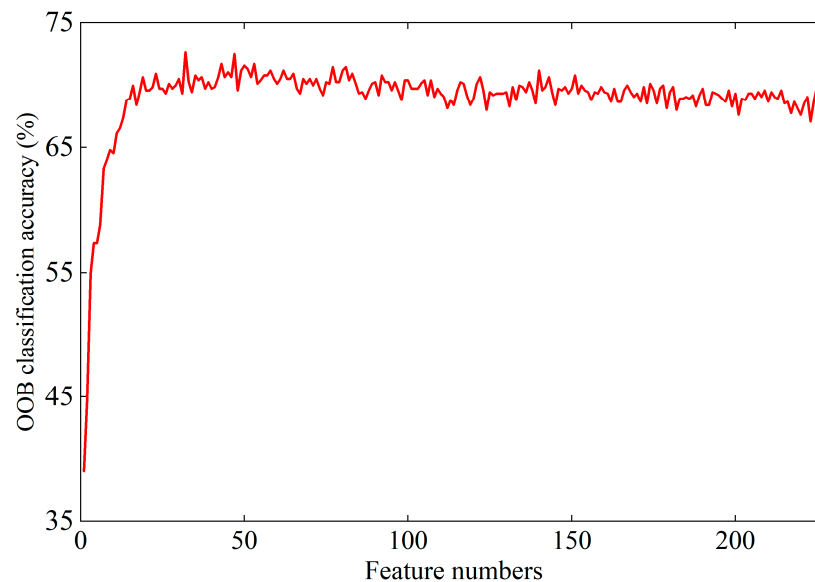


Figure 14. RF OOB classification accuracy with different numbers of S2 features.

For the S2-RF model, as Figure 14 shows, the combination of the first 32 features shows the largest classification accuracy. Thus, the features whose importance ranks between 33rd and 228th are discarded, with the selected and unselected features shown in orange and blue colors, respectively, in Figure 13. According to the importance ranking shown in Figure 13, the texture features (shown in the last two parts) have higher importance in the BFT classification than the spectral features (shown in the first two parts). Twenty-six of the 192 texture features, with an average importance of 0.434, and six of the 36 spectral features, with an average importance of 0.419, are used in the S2-RF model construction. In addition, the 17 features produced from the S2 images of 21 June 2020 are used (shown on gray background) as compared with 15 features from December 8 (shown on white background). This shows that image acquisition time has little effect on the classification performance under this classification scheme.

Finally, the MS-RF model and S2-RF model are constructed based on their corresponding first 23 and 32 features and are used for BFT classification.

5.2. BFT Classification Accuracy Assessment Using MS Data

Taking the BFT of the 30% test samples as a reference, the confusion matrix of the MS-RF model-predicted test samples' BFTs versus reference BFTs is shown in Table 6. The OA indicates that 84.89% of the BFTs were accurately predicted. Producer's accuracy (PA) indicates the probability that the ground-truth classification of the class is correctly predicted. It varies widely for different BFTs. As shown in Table 6, the three BFTs, i.e., *R*, *W*, and *V*, have higher PA values that exceed 80%, and *E* and *H* have lower PA values. This result may be related to the uneven distribution of building numbers in the actual functional types. In urban areas, there are more residential, working, and visiting types of buildings, and more training samples are available and selected for model training. However, as compared with *R*, the number of available training samples of *V* is much smaller, but the classification accuracies of the two BFTs are not considerably different, while the training samples of *W* and *V* are similar in number, but the classification accuracies are more than 10% different. This difference may be related to the typicality of the population dynamics change patterns within BFTs. As compared with that in *W*, the population dynamics change pattern within *V*-type buildings is relative unity (namely, including fewer subtypes), while the BFT of *W*, according to its different types of work, has some small differences in its population dynamics change pattern, which leads to a reduction in the classification accuracy. The confusion matrix indicates that 33.33% of the *H*-type buildings were misclassified as *W*-type buildings. This may be due to the presence of some hospital outpatient clinics, which have a different human mobility pattern as compared with hospitals. Their working hours range is from 9 to 17, which matches that of the *W*-type buildings, and therefore, it leads to a large classification error. User accuracy (UA) is the probability that any random sample from the classification results has the same type as the actual type on the ground. The UA is larger than 72% for all five types, indicating that the types predicted by the classifier are highly matched with the real types. The UA results are not affected by the uneven sample number distribution of different BFTs.

Table 6. Confusion matrix of the MS-RF model-predicted BFTs versus reference BFTs for the test sample set.

	Residential	Working	Entertainment	Visiting	Hospital	UA (%)	OA (%)
Residential	89	6	3	2	1	88.12	
Working	6	36	2	2	4	72.00	
Entertainment	1	0	11	1	0	84.62	
Visiting	1	2	1	49	1	90.74	84.89
Hospital	0	1	0	0	6	85.71	
PA (%)	91.75	80.00	64.70	90.74	50.00		

After analyzing these indicators, the Kappa coefficient is used to evaluate the classification quality. A Kappa analysis is a method to quantitatively evaluate the consistency or accuracy between the classification map and the reference data, and it uses a discrete multivariate approach, overcoming the confusion matrix's overreliance on the sample and sample data collection process. The Kappa coefficient was 0.78, falling between 0.6 and 0.8, indicating a high degree of consistency between the classification results and the true BFTs.

5.3. Comparison with S2 Data

To study the feasibility and superiority of MS data for BFT classification, remote sensing data were also used for BFT prediction for a comparison. In this section, two different RF models (MS-RF and S2-RF) are constructed based on MS and S2 data, respectively.

First, the 750 samples acquired from previous steps were randomly split into two parts, 70% as the training set and 30% as the test set. To avoid the influence of different samples being used for model training and testing, the same training set and test set were used for the training and test process of the MS-RF and S2-RF models. To improve the

objectivity of the prediction results comparison, the upwards process was repeated ten times. Then, the average classification accuracy and standard deviation error bar of 10 independent experiments for the test samples were calculated and plotted in Figure 15. The results for the MS-RF and S2-RF models are shown in blue and orange, respectively. The overall classification accuracy of S2-RF is 73.33%, which is lower than that of the MS-RF model. The accuracy of the classification results of the five individual BFTs based on the MS-RF model are all improved as compared with those of the S2-RF model. In addition, the MS-RF model has a lower error bar (standard deviation for 10 tests) than the S2-RF model for the overall and five individual BFTs. This indicates that the MS-RF model is more stable for BFT prediction, calculated from ten independent experiments.

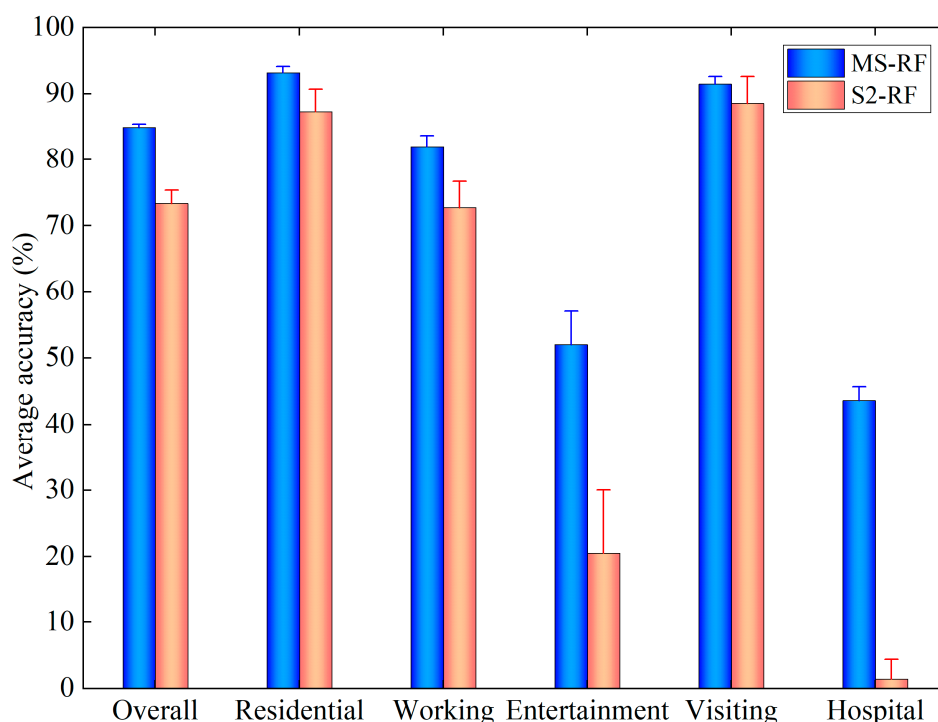


Figure 15. Average and standard deviation of the classification accuracy of the MS-RF model and S2-RF model for ten independent experiments.

Then, to visually represent the differences in classification results between these two datasets, the confusion matrices for the 10 independent experiments with the prediction accuracy ranked 5th are shown in Tables 7 and 8. As seen from them, with identical training and test sets, the PA and UA of all five BFTs based on the MS-RF model are all improved as compared with those of the S2-RF model. The overall classification accuracy of the MS-RF model is 84.89% with a Kappa coefficient of 0.79, while the overall classification accuracy of the S2-RF model is 73.33% with a Kappa coefficient of 0.62.

Table 7. The confusion matrix of the MS-RF model-predicted BFTs for the 10 independent experiments with the prediction accuracy ranked 5th.

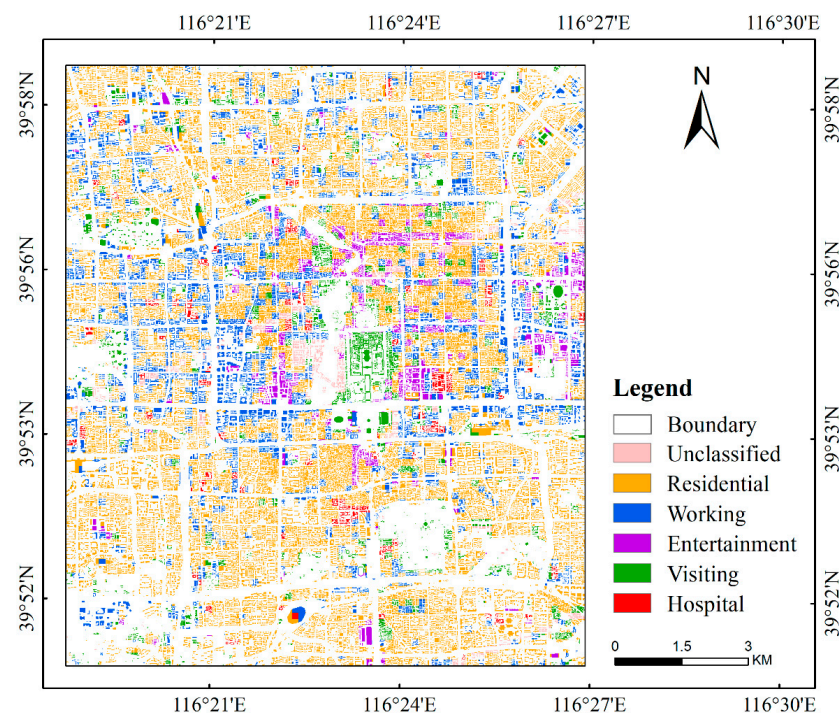
	Residential	Working	Entertainment	Visiting	Hospital	UA (%)	OA (%)
Residential	78	7	6	1	3	82.11	
Working	3	50	4	2	1	83.33	
Entertainment	1	1	10	2	0	71.43	
Visiting	1	2	0	50	0	94.34	84.89
Hospital	0	0	0	0	3	100.00	
PA (%)	93.98	83.33	50.00	90.90	42.86		

Table 8. The confusion matrix of the S2-RF model-predicted BFTs for the 10 independent experiments with the prediction accuracy ranked 5th.

	Residential	Working	Entertainment	Visiting	Hospital	UA (%)	OA (%)
Residential	71	10	4	4	3	77.17	73.33
Working	9	41	9	3	3	63.08	
Entertainment	1	6	4	0	0	36.36	
Visiting	2	3	3	48	0	85.71	
Hospital	0	0	0	0	1	100.00	
PA(%)	85.54	68.33	20.00	87.27	14.29		

5.4. Model Application

After the MS-RF model was constructed, the BFTs of the study area with a total of 70,613 buildings were estimated and are shown in different colors in Figure 16. The overall detection rate (the number of identifiable buildings as a proportion of the total number of buildings in the study area) is 97.35%. Figure 17 shows the percentage of the identified building types of the study region buildings in the count and area of the five BFTs. The count and area are shown in orange and blue, respectively. From Figures 16 and 17, the *R-type* buildings account for the largest proportion, with 58.84% of the count and 55.58% of the area. These buildings are distributed mainly in the area south of Changan Street within the Second Ring Road and outside the Second Ring Road. This building type is followed by *W-type* buildings, accounting for 19.58% of the total count. As compared with *R-type* buildings, *W-type* buildings are mostly decentralized. Classes *E* and *V* are mostly clustered and are concentrated in the central area, which is related to their recreational nature. The predicted results of *E-type* buildings are highly consistent with the commercial areas in Beijing of Xidan, Wangfujing, Qianmen, and Sanlitun. *V* is located mainly around famous tourist attractions such as the Forbidden City, Temple of Heaven, and Yonghe Palace. Those buildings predicted to be *H-type* buildings were almost all correctly classified, but there were still some misclassifications into other categories. The result illustrated that 2.65% of the buildings could not be identified because there were no MS data available for these buildings.

**Figure 16.** RF model-predicted BFT map for the study area.

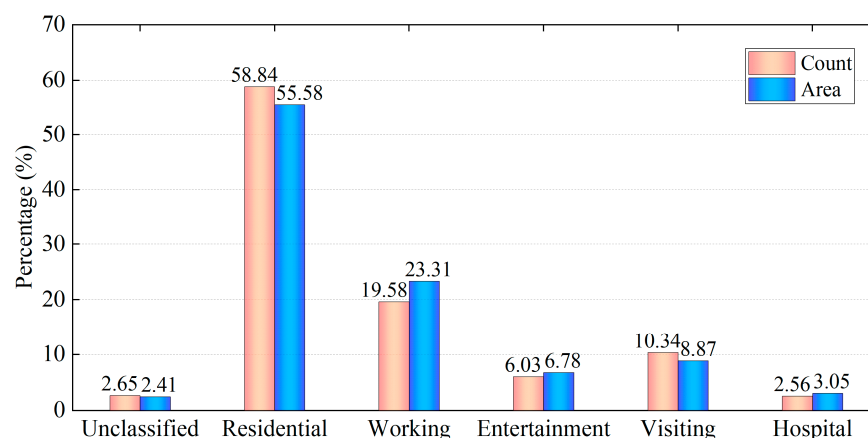


Figure 17. Statistics on the count and area of identified building types in the study area.

To validate the classification results in more detail, a typical region was selected for further evaluation. Figure 18 shows the predicted BFT map of Donghuamen Street, located in the center of the study area. This area contains complex BFTs containing all the main categories of the building function classification system proposed in this study. Therefore, the area is representative for the analysis of BFT classification. This area is divided into three zones for detailed analysis, according to the spatial division of roads. The buildings in Zone A are dominated by the Forbidden City, which is correctly classified as Class V. However, the low-rise residential Beijing hutongs east of the Forbidden City are misclassified as V. During the field research, it was found that because the Forbidden City had a relatively large flow of people and concentrated activity time, the hutongs next to it were significantly affected, many of which had developed tourism-related industries, and thus, were easily misclassified as Class V. However, in reality, in terms of its flow pattern, it does lean more towards category V. Zones B and C are multifunctional zones, with complex building functions and mostly office and entertainment buildings. However, there are several unclassified buildings in Zone C, which are mostly related to the privacy of their building nature.

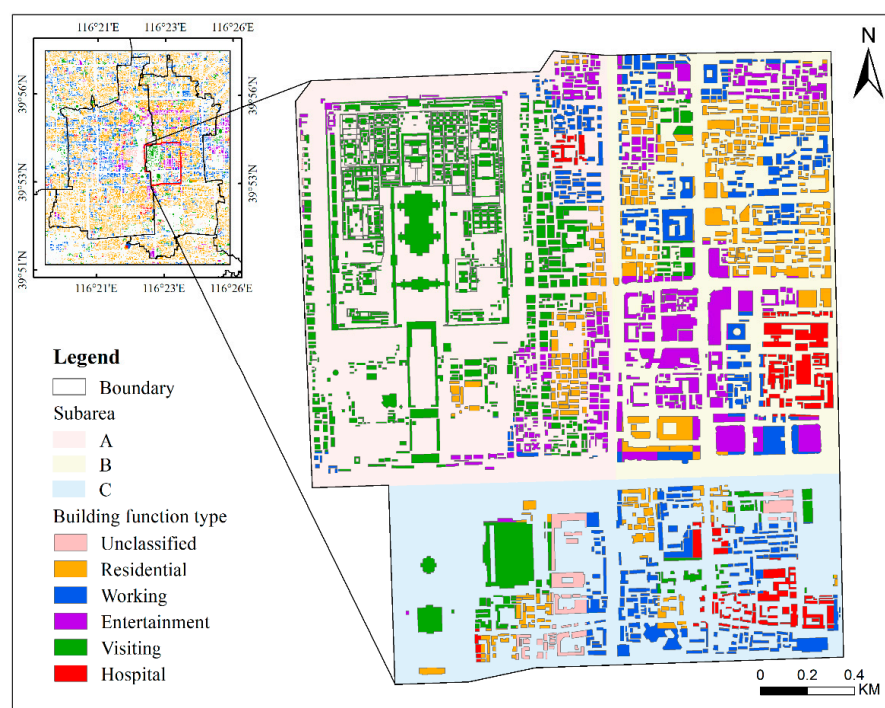


Figure 18. BFT map of Donghuamen Street predicted using the constructed RF models.

To verify the large-scale applicability of this method, we used the proposed model to predict the central urban area of Beijing, as shown in Figure 19. The area is mostly located within the Fifth Ring Road of Beijing, with a total area of 1085 km², seven times larger than the study area. The district is densely populated and densely built, carrying the majority of Beijing's population and building functions. Figure 20 shows the percentage of the identified building types in the main urban center of Beijing in the count and area of the five BFTs. The overall detection rate was 94.74%. There are significant differences in the distribution of the five types of buildings. The largest proportion of buildings is *R*, with a wide and dense distribution, accounting for 55.33% of the total count and 51.08% of the total area. The next most densely distributed buildings are *W* and *V*. *W* is more densely distributed within the Third Ring Road, accounting for 15.62% of the total count and 18.63% of the total area. *V* is relatively evenly distributed throughout the district, with 20.37% in count and 20.39% in area. *E* is mainly distributed within the 2nd Ring Road, with a clear cluster distribution, as compared with *H* which is more evenly distributed.

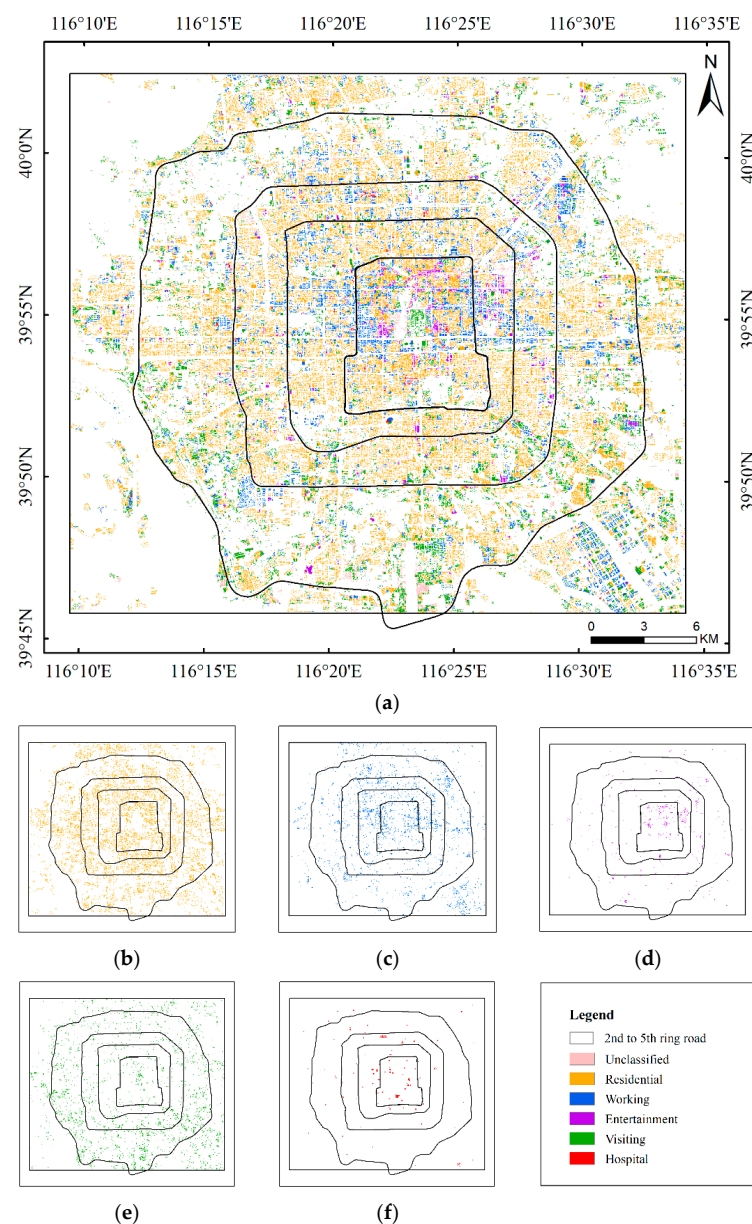


Figure 19. RF model-predicted BFT map for the main urban center of Beijing: (a) All five BFTs; (b) *R*; (c) *W*; (d) *E*; (e) *V*; (f) *H*.

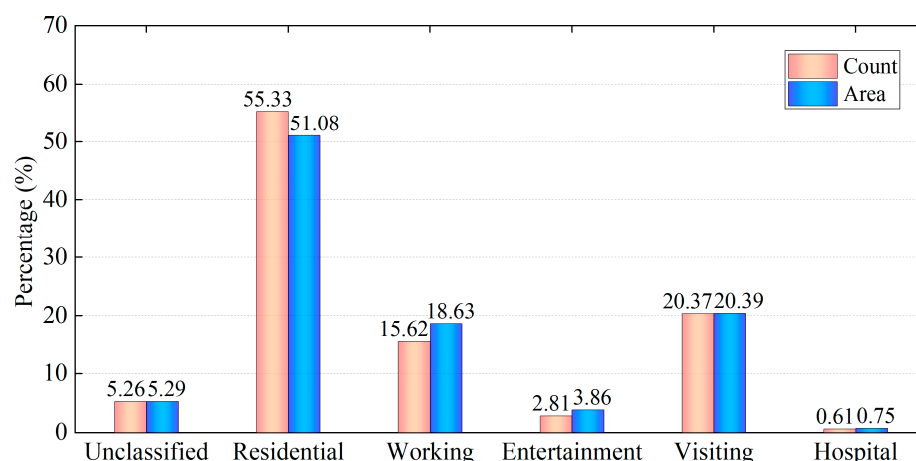


Figure 20. Statistics on the count and area of identified building types in the main central area of Beijing.

6. Discussion

Buildings are the most basic units of urban planning and generally correspond to different patterns of population dynamics. Correct BFT identification is very significant for all urban applications with humans as the most important part. MS data, as emerging social sensing data acquired directly by human sensors, can help to identify detailed building functions on a large scale due to its wide spatial coverage and high temporal resolution.

This study shows the potential of using MS data to study diurnal variations in population dynamics for BFT identification with a spatial resolution of 150 m. As people are required to actively send messages to be recorded, POIs, taxi trajectories, social chat user density, and Twitter text messages commonly have low sample rates. For example, Twitter text messages require people to post a Twitter feed to be recorded. In contrast, MS has a higher sampling rate, as MS records can be recorded as long as mobile devices are being used. Thus, the MS data can reasonably represent human activities with wide spatial coverage and high temporal resolution. However, for diverse MS indicators, such as Station, Gid, Wifimac, and Loginmac, few references are available to understand which indicator can be effectively applied to BFT prediction. Most studies have described such data in general terms, such as phone location signal data [66] or mobile phone records [37], without specifying the specific indicators used. Pang et al. first compared the changes in these four indicators before and after earthquakes, and the results showed that Wifimac and Loginmac had better performance in the rapid determination of earthquake impact fields [33], which was indicative of earthquake emergency response and rescue. However, few studies have compared the performance of these indicators for BFT classification. This study proposed a combined qualitative and quantitative approach to compare the performances of the indicators in different dimensions. The results show that the best performing indicator for BFT classification is Gid, which may be closely related to its flexibility, portability, and wide distribution.

Additionally, based on the existing building classification, this study proposed a BFT classification scheme of five classes driven by different population dynamics. This classification scheme is useful for human activity-driven urban management or natural/anthropogenic disaster emergency responses. Although previous studies have considered the ability of call detail records to reflect the variations in population dynamics [7], they did not consider this new pattern of change-driven functional classification and still followed the traditional classification scheme, resulting in low classification accuracy.

In addition, unlike other studies that have commonly applied population size variations as metrics, this study argues that the absolute population size is always influenced by multiple factors in addition to BFT (such as epidemic control or regional development level) and is not stable, making it less general for large-scale BFT mapping. Therefore, this study

normalized the MS data when exploring the potential of MS to identify BFT. The purpose of this step was to explore the BFT information reflected by its population dynamics variation patterns on each study unit basis. This identification model, which relies on population dynamics variation patterns within buildings rather than population size variations, is more stable and can be more readily generalized to large-scale BFT mapping applications.

In this study, traditional remote sensing methods were used for a comparison to verify the feasibility of MS data for BFT classification. As seen in Figure 15, the overall classification accuracy of MS data is higher in this classification framework. In addition, in the functional classification of actual urban buildings, the differentiation of special categories, such as *E* and *H*, is difficult for remote sensing data, while MS data, with its sensitive detection capability, can be used for BFT identification in the case of extremely uneven urban distributions. This is attributed to the detection mechanism of remote sensing and social sensing data. Remote sensing detection mainly perceives the physical environment based on remote sensing signals obtained from different remote sensing sensors, while social sensing detection directly perceives the socioeconomic environment based on the dynamic behavioral patterns of a population obtained from human sensors. Therefore, as compared with the S2 data-based method, the MS data-based method is more suitable for the BFT classification framework oriented to population dynamics in this study.

There are also some limitations that will be addressed in future work. First, although the resolution of Geohash7 data at 150 m meets the requirement of functional agglomeration of most buildings and ensures the richness of information within the grid, there are still mixed grids due to the complex distribution of urban buildings that leads to some buildings being misclassified as the dominant BFT within the grid. A spatial resolution of 150 m makes it impossible to differentiate the buildings of different BFTs with dimensions of tens of meters. There are cases where a building is segmented into several nearby Geohash grids. In further studies, we plan to use more refined data to estimate BFT. Second, although the overall classification accuracy of the model is as high as 85%, the classification accuracies of buildings in BFT's *E* and *H* are low. This is mainly due to the small proportion of these two BFTs in the building function layout. Namely, there are indeed more *R*-type buildings than *E*- or *H*-type buildings in actual urban or village areas. Although some *E*- and *H*-type buildings (with classification accuracies of 65% and 50%, respectively) can be identified from the extremely heterogeneous urban layout based on the circadian rhythm variation in MS activity, a more sensitive classification method deserves further exploration.

In the future, we plan to apply this method to more cities and to integrate other data sources to use multidisciplinary knowledge to infer BFT more accurately. The practical application of inferred BFTs for earthquake emergency response is one of our next key research directions.

7. Conclusions

Along with the continuous development of urbanization, buildings have become the basic unit to support human activities. The BFT is a key parameter that determines the population distribution at both spatial and temporal scales, as well as green space planning, shelter construction, etc. In recent years, remote sensing- and social sensing-based methods have been proposed for BFT identification at different spatial scales of regions, blocks, or buildings. This study investigated the potential of using MS data for BFT identification with an RF model.

The building footprint layer and the corresponding BFT data from OSM are taken as references for BFT identification model construction. As some of the buildings are ignored in OSM, the buildings are filled in with the help of the street view of Gaode Map. Then, 750 samples are acquired from the study area of Beijing, with all the samples classified into five BFTs based on their population dynamics variation patterns: residential, working, entertainment, visiting, and hospital. Four types of MS data are considered: Station, Gid, Wifimac, and Loginmac. After comparing the prediction performance, Gid is used for BFT prediction. The RF model considering different parameters of leaf numbers and tree

numbers is also used for BFT identification. Taking 70% of the total sample as the training set and the remaining 30% as the test set, the MS data-constructed RF model (MS-RF) has an overall classification accuracy of 84.89% with a leaf number of 1 and tree number of 500. To verify the feasibility of the proposed method, remote sensing data from Sentinel-2 are used for comparison. The classification accuracies of the MS-RF model exceed those of the S2-RF model for all five BFTs. When applying the constructed MS-RF model to the central areas of Beijing Dongcheng and Xicheng Districts, the final detection rate is 97.35%. Later, the model is applied to a larger area of Beijing within the 5th Ring Road, and the overall detection rate reaches 94.74%.

This is the first attempt to use MS data independently for BFT identification. As compared with traditional widely used satellite remote sensing data, time-series MS data have the advantages of being intrinsically more useful for BFT identification, as population spatial and temporal dynamic variations reviewed by MS data are more correlated with BFT than geometric or spectral features in remote sensing images. As compared with other types of social sensing data applying spatial information, the time-series information represented by diurnal and daily (weekday/weekend) patterns in population dynamics is used for BFT identification. In this paper, we validate the feasibility and superiority of using MS data for BFT identification and we provide new ideas for the functional mapping of large-scale urban/village buildings using humanities-based big data. The classification products generated by this study greatly reflect the population dynamics, which has important implications for urban management and risk assessment, such as earthquake emergency rescue, prevention and control of COVID-19, and traffic control.

Author Contributions: Conceptualization, X.F.; methodology, G.N.; software, C.X.; resources, H.L.; writing, W.N. All authors have read and agreed to the published version of the manuscript.

Funding: This research was jointly funded by the National Nonprofit Fundamental Research Grant of China, Institute of Geology, China Earthquake Administration, grant number IGCEA2106 and the National Natural Science Foundation of China, grant number 42071337.

Conflicts of Interest: The authors declare no conflict of interest.

Abbreviations

The following abbreviations are used in this manuscript:

BFT	Building function type
MS	Mobile signaling
R	Residential
W	Working
E	Entertainment
V	Visiting
H	Hospital
RF	Random forest
OA	Overall accuracy
S2	Sentinel-2
Station	Number of active communication stations
Gid	Number of online mobile devices
Wifimac	Number of Active Wi-Fi Hotspots
Loginmac	Number of connected devices in wireless networks
OSM	Open Street Map
POI	Point of interest
SDK	Software development kit
VGI	Volunteered Geographic Information
DS	Data sharing
ESA	European Space Agency
API	Application Programming Interface
TOA	Top-of-atmosphere
BOA	Bottom-of-atmosphere

NDBI	Normalized difference built-up index
MNDWI	Modified normalized difference water index
NDVI	Normalized difference vegetation index
TCB	Tasseled cap brightness
TCG	Tasseled cap greenness
TCW	Tasseled cap wetness
TCT	Tasseled cap transformation
GLCM	Gray level co-occurrence matrix
N	Number of decision trees
L	Number of leaves
OOB	Out-of-bag
MS-RF	Mobile Signaling Random Forest Classification Model
S2-RF	Sentinel-2 Random Forest Classification Model
PA	Producer's accuracy
UA	User accuracy

References

- Tu, W.; Hu, Z.; Li, L.; Cao, J.; Jiang, J.; Li, Q.; Li, Q. Portraying urban functional zones by coupling remote sensing imagery and human sensing data. *Remote Sens.* **2018**, *10*, 141. [[CrossRef](#)]
- Niu, N.; Liu, X.; Jin, H.; Ye, X.; Liu, Y.; Li, X.; Chen, Y.; Li, S. Integrating multi-source big data to infer building functions. *Int. J. Geog. Inf. Sci.* **2017**, *31*, 1871–1890. [[CrossRef](#)]
- Liu, X.; Niu, N.; Liu, X.; Jin, H.; Ou, J. Characterizing mixed-use buildings based on multi-source big data. *Int. J. Geog. Inf. Sci.* **2018**, *32*, 738–756. [[CrossRef](#)]
- Deng, Y.; Chen, R.; Yang, J.; Li, Y.; Jiang, H.; Liao, W.; Sun, M. Identify urban building functions with multisource data: A case study in Guangzhou, China. *Int. J. Geog. Inf. Sci.* **2022**, 1–26. [[CrossRef](#)]
- Xie, J.; Zhou, J. Classification of Urban Building Type from High Spatial Resolution Remote Sensing Imagery Using Extended MRS and Soft BP Network. *IEEE J. Sel. Top. Appl. Earth Obs. Remote Sens.* **2017**, *10*, 3515–3528. [[CrossRef](#)]
- Zhuo, L.; Shi, Q.; Zhang, C.; Li, Q.; Tao, H. Identifying building functions from the spatiotemporal population density and the interactions of people among buildings. *ISPRS Int. J. Geo-Inf.* **2019**, *8*, 247. [[CrossRef](#)]
- Toole, J.L.; Ulm, M.; González, M.C.; Bauer, D. Inferring land use from mobile phone activity. In Proceedings of the ACM SIGKDD International Workshop on Urban Computing—UrbComp '12, Beijing, China, 12 August 2012. [[CrossRef](#)]
- Meżyk, M.; Chamarczuk, M.; Malinowski, M. Automatic Image-Based Event Detection for Large-N Seismic Arrays Using a Convolutional Neural Network. *Remote Sens.* **2021**, *13*, 389. [[CrossRef](#)]
- Harirchian, E.; Jadhav, K.; Kumari, V.; Lahmer, T. ML-EHSAPP: A prototype for machine learning-based earthquake hazard safety assessment of structures by using a smartphone app. *Eur. J. Environ. Civ. Eng.* **2021**, *25*, 1–21. [[CrossRef](#)]
- Su, J.; Bai, Y.; Wang, X.; Lu, D.; Zhao, B.; Yang, H.; Koshimura, S. Technical Solution Discussion for Key Challenges of Operational Convolutional Neural Network-Based Building-Damage Assessment from Satellite Imagery: Perspective from Benchmark xBD Dataset. *Remote Sens.* **2020**, *12*, 3808. [[CrossRef](#)]
- Jane, J. *The Death and Life of Great American Cities*; Eandom House: New York, NY, USA, 1961.
- Rodrigue, J.P.; Comtois, C.; Slack, B. *The Geography of Transport Systems*; Routledge: London, UK, 2013. [[CrossRef](#)]
- Zhong, C.; Huang, X.; Müller Arisona, S.; Schmitt, G.; Batty, M. Inferring building functions from a probabilistic model using public transportation data. *Comput. Environ. Urban Syst.* **2014**, *48*, 124–137. [[CrossRef](#)]
- Lu, Z.; Im, J.; Rhee, J.; Hodgson, M. Building type classification using spatial and landscape attributes derived from LiDAR remote sensing data. *Landsc. Urban Plann.* **2014**, *130*, 134–148. [[CrossRef](#)]
- Du, S.; Zhang, F.; Zhang, X. Semantic classification of urban buildings combining VHR image and GIS data: An improved random forest approach. *ISPRS J. Photogramm. Remote Sens.* **2015**, *105*, 107–119. [[CrossRef](#)]
- Hu, Q.; Zhen, L.; Mao, Y.; Zhou, X.; Zhou, G. Automated building extraction using satellite remote sensing imagery. *Autom. Constr.* **2021**, *123*, 103509. [[CrossRef](#)]
- Hoffmann, E.J.; Wang, Y.; Werner, M.; Kang, J.; Zhu, X. Model Fusion for Building Type Classification from Aerial and Street View Images. *Remote Sens.* **2019**, *11*, 1259. [[CrossRef](#)]
- Cerovecki, A.; Gharahjeh, S.; Harirchian, E.; Ilin, D.; Okhotnikova, K.; Kersten, J. Evaluation of Change Detection Techniques using Very High Resolution Optical Satellite Imagery. *Preface* **2015**, *2*, 20.
- Gašparović, M.; Jogun, T. The effect of fusing Sentinel-2 bands on land-cover classification. *Int. J. Remote Sens.* **2017**, *39*, 822–841. [[CrossRef](#)]
- Ruiz Hernandez, I.E.; Shi, W. A Random Forests classification method for urban land-use mapping integrating spatial metrics and texture analysis. *Int. J. Remote Sens.* **2017**, *39*, 1175–1198. [[CrossRef](#)]
- Zhang, C.; Sargent, I.; Pan, X.; Li, H.; Gardiner, A.; Hare, J.; Atkinson, P.M. An object-based convolutional neural network (OCNN) for urban land use classification. *Remote Sens. Environ.* **2018**, *216*, 57–70. [[CrossRef](#)]

22. Haghghattalab, A.; Mohammadzadeh, A.; Zoej, M.J.V. Post-earthquake road damage assessment using region-based algorithms from high-resolution satellite images. *Proc. SPIE* **2010**, *7830*, 439–447. [[CrossRef](#)]
23. Belgiu, M.; Tomljenovic, I.; Lampoltshammer, T.J.; Blaschke, T.; Höfle, B. Ontology-based classification of building types detected from airborne laser scanning data. *Remote Sens.* **2014**, *6*, 1347–1366. [[CrossRef](#)]
24. Chen, W.; Zhou, Y.; Wu, Q.; Chen, G.; Huang, X.; Yu, B. Urban Building Type Mapping Using Geospatial Data: A Case Study of Beijing, China. *Remote Sens.* **2020**, *12*, 2805. [[CrossRef](#)]
25. Ilieva, R.T.; McPhearson, T. Social-media data for urban sustainability. *Nat. Sustain.* **2018**, *1*, 553–565. [[CrossRef](#)]
26. Shaw, S.L.; Tsou, M.H.; Ye, X. Editorial: Human dynamics in the mobile and big data era. *Int. J. Geog. Inf. Sci.* **2016**, *30*, 1687–1693. [[CrossRef](#)]
27. Zhang, X.; Li, W.; Zhang, F.; Liu, R.; Du, Z. Identifying Urban Functional Zones Using Public Bicycle Rental Records and Point-of-Interest Data. *ISPRS Int. J. Geo-Inf.* **2018**, *7*, 459. [[CrossRef](#)]
28. Lin, A.; Sun, X.; Wu, H.; Luo, W.; Wang, D.; Zhong, D.; Wang, Z.; Zhao, L.; Zhu, J. Identifying Urban Building Function by Integrating Remote Sensing Imagery and POI Data. *IEEE J. Sel. Top. Appl. Earth Obs. Remote Sens.* **2021**, *14*, 8864–8875. [[CrossRef](#)]
29. Häberle, M.; Hoffmann, E.J.; Zhu, X. Can linguistic features extracted from geo-referenced tweets help building function classification in remote sensing? *ISPRS J. Photogramm. Remote Sens.* **2022**, *188*, 255–268. [[CrossRef](#)]
30. Zhong, Y.; Su, Y.; Wu, S.; Zheng, Z.; Zhao, J.; Ma, A.; Zhu, Q.; Ye, R.; Li, X.; Pellikka, P.; et al. Open-source data-driven urban land-use mapping integrating point-line-polygon semantic objects: A case study of Chinese cities. *Remote Sens. Environ.* **2020**, *247*, 111838. [[CrossRef](#)]
31. Gong, P.; Chen, B.; Li, X.; Liu, H.; Wang, J.; Bai, Y.; Chen, J.; Chen, X.; Fang, L.; Feng, S.; et al. Mapping essential urban land use categories in China (EULUC-China): Preliminary results for 2018. *Sci. Bull.* **2020**, *65*, 182–187. [[CrossRef](#)]
32. Tu, W.; Zhu, T.; Xia, J.; Zhou, Y.; Lai, Y.; Jiang, J.; Li, Q. Portraying the spatial dynamics of urban vibrancy using multisource urban big data. *Comput. Environ. Urban Syst.* **2019**, *80*, 101428. [[CrossRef](#)]
33. Pang, X.; Nie, G.; Zhang, X.; Li, H.; Xia, C.; Fan, X.; Wei, B. Selection of earthquake disaster indicators based on cell phone location data. *Earthq. Res. China* **2019**, *35*, 144–157.
34. Gonzalez, M.C.; Hidalgo, C.A.; Barabasi, A.L. Understanding individual human mobility patterns. *Nature* **2008**, *453*, 779–782. [[CrossRef](#)] [[PubMed](#)]
35. Song, C.; Qu, Z.; Blumm, N.; Barabási, A.L. Limits of predictability in human mobility. *Science* **2020**, *327*, 1018–1021. [[CrossRef](#)]
36. Zhai, Y.; Wu, H.; Fan, H.; Wang, D. Using mobile signaling data to exam urban park service radius in Shanghai: Methods and limitations. *Comput. Environ. Urban Syst.* **2018**, *71*, 27–40. [[CrossRef](#)]
37. Li, D.; Chen, H.; Shen, W.; Ye, M. An analysis of the temporal and spatial gathering and dispersion patterns of crowds at the community level after the 2020 M5.1 Tangshan Guye earthquake. *Int. J. Disaster Risk Reduct.* **2021**, *61*, 102331. [[CrossRef](#)]
38. Xia, C.; Nie, G.; Fan, X.; Zhou, J. Research on the estimation of the real-time population in an earthquake area based on phone signals: A case study of the Jiuzhaigou earthquake. *Earth Sci. Inf.* **2019**, *13*, 83–96. [[CrossRef](#)]
39. Montgomery, J. Making a city: Urbanity, vitality and urban design. *J. Urban Des.* **1998**, *3*, 93–116. [[CrossRef](#)]
40. Tu, W.; Cao, J.; Yue, Y.; Shaw, S.L.; Zhou, M.; Wang, Z.; Chang, X.; Xu, Y.; Li, Q. Coupling mobile phone and social media data: A new approach to understanding urban functions and diurnal patterns. *Int. J. Geo-Inf. Sci.* **2017**, *31*, 2331–2358. [[CrossRef](#)]
41. Agard, B.; Morency, C.; Trépanier, M. Mining public transport user behaviour from smart card data. In Proceedings of the 12th IFAC Symposium on Information Control Problems in Manufacturing—INCOM 2006, Saint-Etienne, France, 17–19 May 2006. [[CrossRef](#)]
42. Bagchi, M.; White, P.R. The potential of public transport smart card data. *Transp. Policy* **2005**, *12*, 464–474. [[CrossRef](#)]
43. Liu, L.; Hou, A.; Biderman, A.; Ratti, C.; Chen, J. Understanding individual and collective mobility patterns from smart card records: A case study in Shenzhen. In Proceedings of the 12th International IEEE Conference on Intelligent Transportation Systems, St. Louis, MI, USA, 3–7 October 2009. [[CrossRef](#)]
44. Park, J.Y.; Kim, D.J.; Lim, Y. Use of smart card data to define public transit use in Seoul/South Korea. *Transp. Res. Rec.* **2008**, *2063*, 3–9. [[CrossRef](#)]
45. Harirchian, E.; Lahmer, T.; Rasulzade, S. Earthquake hazard safety assessment of existing buildings using optimized multi-layer perceptron neural network. *Energies* **2020**, *13*, 2060. [[CrossRef](#)]
46. Valentijn, T.; Margutti, J.; van den Homberg, M.; Laaksonen, J. Multi-Hazard and Spatial Transferability of a CNN for Automated Building Damage Assessment. *Remote Sens.* **2020**, *12*, 2839. [[CrossRef](#)]
47. Kavzoglu, T.; Colkesen, I. A kernel functions analysis for support vector machines for land cover classification. *Int. J. Appl. Earth Obs. Geoinf.* **2009**, *11*, 352–359. [[CrossRef](#)]
48. Kranjčić, N.; Medak, D.; Župan, R.; Rezo, M. Support Vector Machine Accuracy Assessment for Extracting Green Urban Areas in Towns. *Remote Sens.* **2019**, *11*, 655. [[CrossRef](#)]
49. Breiman, L. Random forests. *Mach. Learn.* **2001**, *45*, 5–32. [[CrossRef](#)]
50. Belgiu, M.; Drăguț, L. Random forest in remote sensing: A review of applications and future directions. *ISPRS J. Photogramm. Remote Sens.* **2016**, *114*, 24–31. [[CrossRef](#)]
51. Haklay, M. How good is volunteered geographical information? A comparative study of OpenStreetMap and ordnance survey datasets. *Environ. Plan. B* **2014**, *37*, 682–703. [[CrossRef](#)]

52. Hong, Y.; Yao, Y. Hierarchical community detection and functional area identification with OSM roads and complex graph theory. *Int. J. Geog. Inf. Sci.* **2019**, *33*, 1569–1587. [[CrossRef](#)]
53. Li, X.; Wang, L.; Cheng, Q.; Wu, P.; Gan, W.; Fang, L. Cloud removal in remote sensing images using nonnegative matrix factorization and error correction. *ISPRS J. Photogramm. Remote Sens.* **2019**, *148*, 103–113. [[CrossRef](#)]
54. Zhu, Z.; Wang, S.; Woodcock, C.E. Improvement and expansion of the Fmask algorithm: Cloud, cloud shadow, and snow detection for Landsats 4–7, 8, and Sentinel 2 images. *Remote Sens. Environ.* **2015**, *159*, 269–277. [[CrossRef](#)]
55. Zhang, Y.; Qin, K.; Bi, Q.; Cui, W.; Li, G. Landscape patterns and building functions for urban land-use classification from remote sensing images at the block level: A case study of Wuchang district, Wuhan, China. *Remote Sens.* **2020**, *12*, 1831. [[CrossRef](#)]
56. Ratti, C.; Richens, P. Urban texture analysis with image processing techniques. In Proceedings of the Eighth International Conference on Computer Aided Architectural Design Futures held at Georgia Institute of Technology, Atlanta, GA, USA, 7–8 June 1999. [[CrossRef](#)]
57. Pesaresi, M. Texture Analysis for Urban Pattern Recognition Using Fine-resolution Panchromatic Satellite Imagery. *Geogr. Environ. Model* **2000**, *4*, 43–63. [[CrossRef](#)]
58. Dekker, R.J. Texture analysis and classification of ERS SAR images for map updating of urban areas in the Netherlands. *IEEE Trans. Geosci. Remote Sens.* **2003**, *41*, 1950–1958. [[CrossRef](#)]
59. Duque, J.C.; Patino, J.E.; Ruiz, L.A.; Pardo-Pascual, J.E. Measuring intra-urban poverty using land cover and texture metrics derived from remote sensing data. *Landsc. Urban Plann.* **2015**, *135*, 11–21. [[CrossRef](#)]
60. Haralick, R.M.; Shanmugam, K.; Dinstein, I. Textural Features of Image Classification. *IEEE Trans. Syst. Man Cybern.* **1973**, *3*, 610–621. [[CrossRef](#)]
61. Anys, H.; Bannari, A.; He, D.; Morin, D. Cartographie des zones urbaines à l'aide des images aéroportées MEIS-II. *Int. J. Remote Sens.* **1998**, *19*, 883–894. [[CrossRef](#)]
62. Breiman, L. Bagging predictors. *Mach. Learn.* **1996**, *24*, 123–140. [[CrossRef](#)]
63. Rodriguez-Galiano, V.F.; Ghimire, B.; Rogan, J.; Chica-Olmo, M.; Rigol-Sanchez, J.P. An assessment of the effectiveness of a random forest classifier for land-cover classification. *ISPRS J. Photogramm. Remote Sens.* **2012**, *67*, 93–104. [[CrossRef](#)]
64. Hughes, G. On the mean accuracy of statistical pattern recognizers. *IEEE Trans. Inf. Theory* **1968**, *14*, 55–63. [[CrossRef](#)]
65. Adelabu, S.; Mutanga, O.; Adam, E. Evaluating the impact of red-edge band from Rapideye image for classifying insect defoliation levels. *ISPRS J. Photogramm. Remote Sens.* **2014**, *95*, 34–41. [[CrossRef](#)]
66. Xia, C.; Nie, G.; Fan, X.; Zhou, J.; Pang, X. Research on the application of mobile phone location signal data in earthquake emergency work: A case study of Jiuzhaigou earthquake. *PLoS ONE* **2019**, *14*, e0215361. [[CrossRef](#)]